





## RESEARCH ARTICLE

10.1029/2022SW003044

### Special Section:

NOAA's Space Weather  
Missions and Instruments

## The GOES-R Solar UltraViolet Imager

Jonathan M. Darnel<sup>1,2</sup> , Daniel B. Seaton<sup>1,2,3</sup> , Christian Bethge<sup>1,2</sup>, Laurel Rachmeler<sup>2</sup>, Alison Jarvis<sup>1,2</sup>, Steven M. Hill<sup>4</sup>, Courtney L. Peck<sup>1,2</sup>, J. Marcus Hughes<sup>3</sup>, Jason Shapiro<sup>1,2</sup>, Allyssa Riley<sup>1,2</sup>, Gopal Vasudevan<sup>5</sup>, Lawrence Shing<sup>5</sup>, George Koener<sup>5</sup>, Chris Edwards<sup>5</sup>, Dnyanesh Mathur<sup>5</sup>, and Shelbe Timothy<sup>5</sup>

<sup>1</sup>Cooperative Institute for Research in Environmental Sciences, University of Colorado, Boulder, CO, USA, <sup>2</sup>National Centers for Environmental Information, National Oceanic and Atmospheric Administration, Boulder, CO, USA, <sup>3</sup>Southwest Research Institute, Boulder, CO, USA, <sup>4</sup>Space Weather Prediction Center, National Oceanic and Atmospheric Administration, Boulder, CO, USA, <sup>5</sup>Lockheed Martin Advanced Technology Center, Palo Alto, CA, USA

### Key Points:

- There are four identically designed Solar UltraViolet Imager (SUVI) instruments hosted on National Oceanic and Atmospheric Administration's Geostationary Operational Environmental satellites
- Each SUVI instrument produces low-latency, high-dynamic-range images of the corona with a relatively large field of view
- The four SUVI instruments will create an extended data of Extreme UltraViolet solar imagery spanning nearly two solar cycles

### Correspondence to:

J. M. Darnel,  
[Jonathan.Darnel@noaa.gov](mailto:Jonathan.Darnel@noaa.gov)

### Citation:

Darnel, J. M., Seaton, D. B., Bethge, C., Rachmeler, L., Jarvis, A., Hill, S. M., et al. (2022). The GOES-R Solar UltraViolet Imager. *Space Weather*, 20, e2022SW003044. <https://doi.org/10.1029/2022SW003044>

Received 24 JAN 2022  
Accepted 17 MAR 2022

**Abstract** The four Solar Ultraviolet Imagers (SUVI) on board the Geostationary Operational Environmental Satellite (GOES)-16 and GOES-17 and the upcoming GOES-T and GOES-U weather satellites serve as National Oceanic and Atmospheric Administration's operational solar coronal imagers. These four identically designed solar Extreme UltraViolet instruments are similar in design and capability to the Solar Dynamics Observatory-Atmospheric Imaging Assembly suite of solar telescopes, and are planned to operationally span two solar cycles or more, from 2017 through 2040. We present the concept of operations for the SUVI instruments, operational requirements, and constraints. The reader is also introduced to the instrument design, testing, and performance characteristics. Finally, the various data products are described along with their potential utility to the operational user or researcher.

**Plain Language Summary** There are four Solar Ultraviolet Imager (SUVI) instruments, one manifested aboard each of the Geostationary Operational Environmental Satellite (GOES)-R series of satellites. The first SUVI instrument aboard GOES-16 began operations in 2017 and a second SUVI instrument on GOES-17 in 2019. These are currently providing forecasters with near-real time solar Extreme UltraViolet (EUV) observations. The GOES-R mission plan ([https://www.nesdis.noaa.gov/s3/2022-01/GEO-Flyout-December-2021\\_signed.pdf](https://www.nesdis.noaa.gov/s3/2022-01/GEO-Flyout-December-2021_signed.pdf)) has at least one SUVI instrument in operations until or beyond 2040. The SUVI data set will therefore span nearly two solar cycles with consistent solar EUV image observations.

## 1. Introduction

The Solar UltraViolet Imager (SUVI) is a new instrument aboard the National Oceanic and Atmospheric Administration's (NOAA) latest series of satellites in the Geostationary Operational Environmental Satellite (GOES) mission. The SUVI instruments, manufactured by Lockheed Martin, are a series of four nearly identical solar imaging telescopes operating in the extreme ultraviolet portion of the solar spectrum. These instruments represent the latest step in NOAA's continuing space weather mission to monitor the solar corona, a mission that began in 2001 with the GOES Solar X-ray Imagers (Hill et al., 2005; Lemen et al., 2012). GOES-16, the first of the GOES-R series of satellites, was successfully launched on 2016 November 19 and achieved geostationary orbit on 29 November 2016. GOES-16 occupies the GOES-East orbital position and began its operational mission on 17 December 2017. GOES-17 successfully launched on 1 March 2018 and achieved geostationary orbit on 12 March 2018. GOES-17 occupies the GOES-West orbital position and began its operational mission on 12 February 2019. There are four satellites planned in the GOES-R series, with GOES-T having launched on 1 March 2022 (now GOES-18) and GOES-U slated to be launched in December 2024. The GOES-R series is currently planned to continuously operate through 2040, providing the scientific and forecasting communities with over two decades of continuous Extreme UltraViolet (EUV) solar observations taken by at least one SUVI instrument. A graphical overview of the GOES-R missions, the different spacecraft, and the planned mission lifetimes can be found at [https://www.nesdis.noaa.gov/s3/2022-01/GEO-Flyout-December-2021\\_signed.pdf](https://www.nesdis.noaa.gov/s3/2022-01/GEO-Flyout-December-2021_signed.pdf).

The GOES satellites' Earth-facing mission provides continuous observations of clouds; atmospheric moisture and temperature; vegetation coverage; snow and ice coverage; fog; smoke; and volcanic ash along with real-time lightning mapping for use in terrestrial weather forecasting. The GOES satellites also monitor solar conditions and the near-Earth space environment, and carry space weather instrumentation that provide continuous in-situ

© 2022 The Authors.

This is an open access article under the terms of the [Creative Commons Attribution-NonCommercial License](https://creativecommons.org/licenses/by-nc/4.0/), which permits use, distribution and reproduction in any medium, provided the original work is properly cited and is not used for commercial purposes.

**Table 1**  
*Solar UltraViolet Imager Spectral Channels*

Peak wavelength (Å)	Notable solar features	Space weather impact
94	Active region solar flare	Thermospheric heating flare warnings fast solar wind
131	Solar flare quiet corona	Thermospheric heating flare warnings
171	Transition region quiet corona	Thermospheric heating active region complexity
195	Active region solar flare coronal hole	Thermospheric heating active region complexity fast solar wind
284	Active region	Thermospheric heating flare warning
304	Chromosphere prominences filament active region	CME warning filament eruption CME forecasting

and remote sensing data. SUVI is an EUV telescope that images the Sun in six narrow spectral bands (94, 131, 171, 195, 284, 304 Å) and greatly expands NOAA's capabilities to characterize solar features and detect events that might affect space weather at Earth and the nearby space environment.

In this paper, we introduce the SUVI instrument, its capabilities, operational concepts, scientific value, and available data products. The following sections will present details of the instrument design and hardware, the results of pre-flight testing, and processing of publicly available Level-1b and Level-2 data products. We will also discuss the value of the SUVI data to the scientific community, methods of acquiring data and the differences between various data sets, and a brief overview of higher-level products of potential interest.

### 1.1. Operational Purpose

The Space Weather Prediction Center (SWPC), part of the National Weather Service (NWS), has the mission of safeguarding society with actionable space weather information. In this role, SWPC with NWS, sets the operational requirements for space weather observations, including SUVI, on the GOES satellites. A key capability for SUVI is to be able to identify features and solar dynamic events that drive space weather events (Arge & Pizzo, 2000) such as coronal holes, for the high-speed solar wind, and active regions and filaments for flares and eruptive events. SUVI is required to provide solar imagery in a sufficient number of spectral bands to enable forecasters to identify and distinguish the solar features of interest: active regions, flaring regions, prominences, filaments, and coronal holes (Table 1). Thus far, the SUVI instruments have met all of their operational and performance requirements (<https://www.goes-r.gov/syseng/docs/MRD.pdf>). For NOAA, the SUVI instruments represent both an advancement and paradigm shift in solar imagery capabilities with regards to image resolution, temperature discrimination, and dynamic range from the prior series of Solar X-Ray Imagers (Hill et al., 2005) flown on the GOES-NOP satellites. Further discussion of the driving requirements for NOAA's solar imagery instrumentation can be found in Hill et al. (2005).

The compact design of SUVI allows it to be placed easily upon the Solar Pointing Platform (SPP) attached to the solar array yoke. SUVI shares the platform and is co-aligned with the Extreme Ultraviolet and X-ray Irradiance Sensors (EXIS; Chamberlin et al., 2009; Eparvier et al., 2009) for all satellites in the GOES-R series, and will additionally share the GOES-U platform with a compact coronagraph CCOR (<https://www.goes-r.gov/space-segment/CCOR.html>). SUVI and EXIS record complementary observations of the EUV and X-ray Sun to keep SWPC forecasters informed of the current solar conditions and events.

SUVI is designed to allow for observation and discrimination of these solar coronal phenomena based on emission wavelength and intensity. For this reason, six spectral channels, centered around prominent EUV emission lines, were selected to cover the temperatures of solar phenomena that can lead to space weather impacts on the Earth. This is reflected by the temperature response functions of the SUVI instruments (see Figure 1). Flaring events are dominated by plasma temperatures in excess of  $10^7$  K, coronal loops in the  $10^6$  K range, and filaments and coronal prominences primarily around  $10^5$  K. SUVI must be sensitive enough to detect the fainter coronal features, but also robust enough to capture the most energetic events without saturating. Handling this dynamic range issue is resolved through a combination of hardware design and operational philosophy.

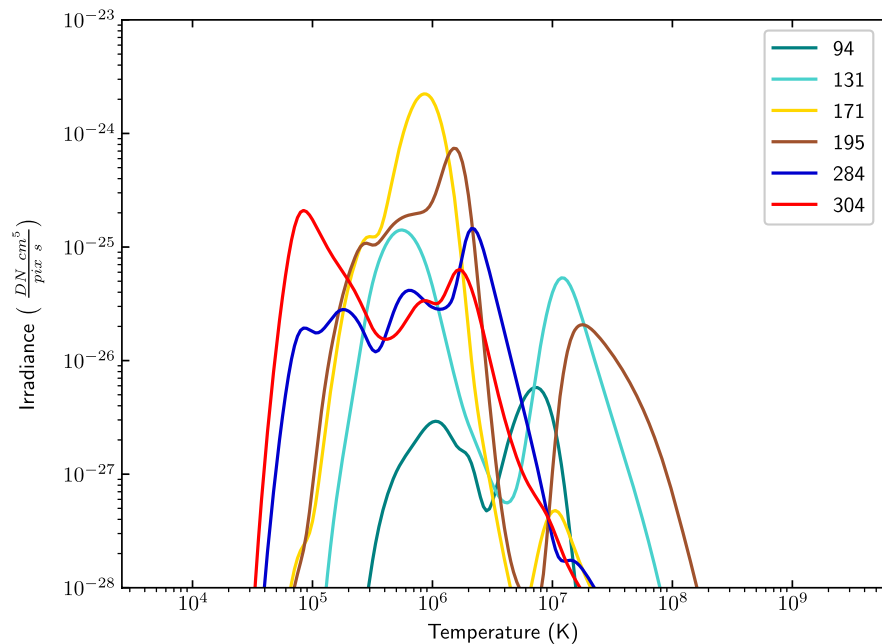


**Figure 1.** The Solar UltraViolet Imager (SUVI) temperature response functions showing the sensitivity of each SUVI channel to temperature-based solar plasma emission. The solar coronal plasma properties used to create this figure are consistent with those used in Section 2.1.

In order to cover the entire required dynamic range, SUVI utilizes a novel 4-min imaging sequence that includes long and short (1 s and 5 milliseconds, respectively) exposure times. The long exposures capture the fainter solar features, and the short exposures are intended to capture the brightest and most energetic solar events (X-flares) without saturating. The channels that are most sensitive to high-temperature solar plasma (the 94 and 131 Å channels) include an additional short exposure with a second focal-plane filter for further signal attenuation. This imaging sequence ensures that SUVI can fully capture all the solar features and events required including fainter solar features such as off-limb prominences and on-disk coronal holes at high signal-to-noise.

SUVI automatically performs key calibration observations when necessary—often scheduled periodically—and can diverge temporarily from its operational sequence to obtain them. Operational needs require that at least one SUVI instrument observes the Sun continuously. However, as a consequence of the geostationary orbit, the GOES satellites experience eclipse seasons around the equinoxes when Earth's equatorial plane and the ecliptic intersect along the Earth-Sun line. During these periods, the GOES satellites are carried into Earth's shadow around local midnight. This leads to an interruption of SUVI observations lasting at most 72 min. During these eclipse or calibration periods the two in-service GOES platforms on-orbit are utilized to ensure continuity of observations and operations.

## 1.2. Instrument Design

### 1.2.1. Instrument Hardware

SUVI is a generalized Cassegrain telescope (Figure 2), a common design used in space-based applications that require a long focal length within a relatively compact space. In such telescopes the observed light is focused using a concave hyperbolic primary mirror and a convex hyperbolic secondary mirror, thus allowing for a very compact design. SUVI's design ensures a high-quality, well-focused image over its entire focal plane, minimizing optical artifacts and aberrations while retaining a compact design (Martínez-Galarce et al., 2013; Seaton & Darnel, 2018).

The novel design of SUVI integrates six spectral EUV channels into a single telescope. SUVI is similar in design to the telescope designs of the Solar Dynamics Observatory's (SDO) Atmospheric Imaging Assembly (AIA; Lemen et al., 2012), the Solar and Heliospheric Observatory's (SOHO) Extreme-ultraviolet Imaging Telescope

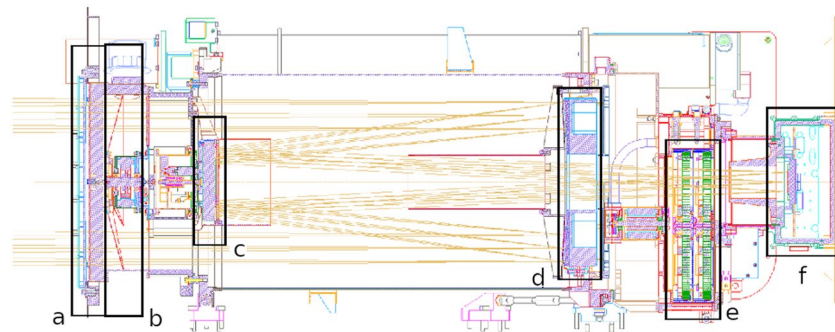


**Figure 2.** Solar UltraViolet Imager (SUVI) optical layout. (a) Entrance aperture, (b) aperture selector, (c) secondary mirror, (d) primary mirror, (e) dual filterwheels, and (f) charge-coupled device block.

(EIT; Delaboudiniere et al., 1995), and the Solar Terrestrial Relations Observatory's (STEREO) Extreme Ultra-Violet Imager (EUVI; Howard et al., 2008), not only optical layout but also in the utilization of segmented mirror pairs. The selection of SUVI's spectral channels overlaps the spectral coverage of AIA, EIT, and EUVI. SUVI is an  $f/9.1$  generalized Cassegrain telescope with primary and secondary Ritchey-Chrétien mirrors with the detector placed at the Cassegrain focus. The SUVI has a 20 cm primary mirror subdivided into six segments, each associated with a specific EUV channel.

The spectral response function for each channel is primarily determined by the reflectivity function of the mirror pairs—The entrance and focal plane filters mainly serve to reject out-of-band photons and have broad spectral throughput compared to the mirrors. The mirrors are designed to utilize constructive interference through multilayer mirror coatings to maximize reflectivity at the desired wavelengths. Each of the primary and secondary mirrors are segmented into six sectors, one for each SUVI channel (Martínez-Galarce et al., 2013). Each sector was individually coated with materials, thicknesses, and the number of layers to tune the channel's spectral response function appropriately (Table 2). An aperture selector allows paired sectors on the primary and secondary mirror to be illuminated during operation.

The entrance and focal plane filters are thin film filters comprised of aluminum or zirconium supported by a stainless steel mesh. As stated previously, the primary function of the filters is visible-light rejection and attenuation of out-of-band signal. The aperture selector determines the set of filters that may be inserted into the optical path. These attenuation filters are located on two filter wheels near the focal plane. Nominal filter combinations are found in Table 6, though we note that other combinations are possible and might be used in the future for the purposes of light leak mitigation or to correct long-term signal attenuation due to contamination. The stainless steel mesh on the entrance filters is known to cause diffraction at the focal plane, and is taken into consideration for the calculated point-spread function (discussed further in Section 2.2). The mesh for the focal plane filters creates a shadow pattern that can be seen in the unprocessed SUVI products. This patterning is removed by applying the flat field correction during the Level-1b production process.

SUVI uses a back-illuminated charge-coupled device (CCD) for its camera, a design that is widely used in astronomical applications due to their favorable signal-to-noise performance even in low-light conditions. SUVI's CCD imaging field-of-view comprises  $1280 \times 1280$  pixels, surrounded by rows and columns of overscan, extended (non-imaging) pixels, and termination pixels (Figure 3). Each pixel subtends a  $2.5$  arcsec square of sky. This provides SUVI with a total field-of-view of about 53 square arcminutes, larger than most EUV near-Earth solar synoptic imagers except for the PROBA2-SWAP instrument (Seaton, Berghmans, et al., 2013), and similar to the Extreme Ultraviolet Imagers (Howard et al., 2008) on the STEREO spacecraft.

It is worth noting that The Solar Orbiter EUV Full Sun Imager (Rochus et al., 2020) can observe out to heights of about  $5 R_{\odot}$  at aphelion, but does not provide synoptic imaging capabilities. The Sun Coronal Ejection Tracker (SunCET) CubeSat EUV imager (Mason et al., 2021), currently in

**Table 2**  
Solar UltraViolet Imager Mirror MultiLayer Configuration

Peak wavelength (Å)	Multilayer composition	Number of layer pairs	Entrance filter type
93.9	Mo/Y	60	Zr
131.2	Mo/Si	25	Zr
171.1	Mo/Si	20	Al
195.1	Mo/Si	20	Al
284.2	Mo/Si	10	Al
303.8	Mo/Si	10	Al

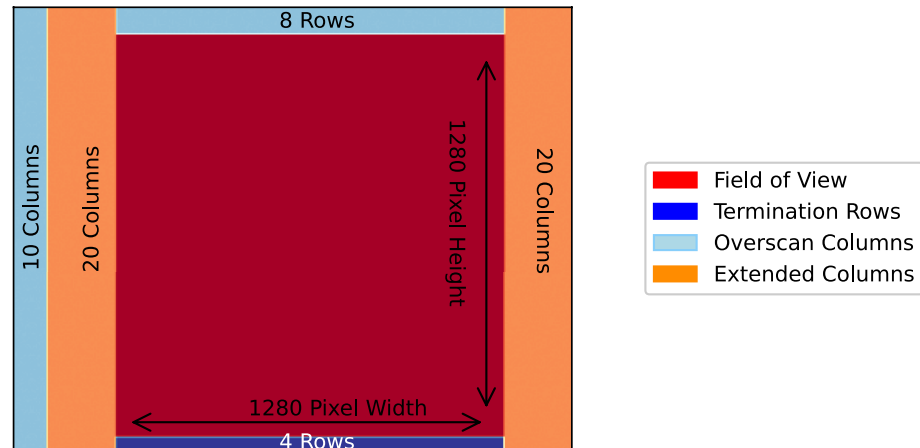


**Figure 3.** The layout of the Solar UltraViolet Imager charge-coupled device.

development, will provide broad-band EUV images of the corona to heights greater than  $4 R_{\odot}$ . Both FSI and SunCET instruments have leveraged SUVI's pioneering off-point observations (see Section 4.1) to help characterize instrument performance during their development phases.

An important feature of SUVI's CCD is its anti-blooming protection, which prevents extremely bright signals in one pixel from spilling over into the pixel's neighbors. This is a common behavior in scientific CCDs without anti-blooming protection and large regions of the image will become obscured during important events that produce very bright phenomena, such as solar flares. Anti-blooming protection ensures that even when a pixel registers a signal that exceeds the limit of its recording range, or saturates, the signal in neighboring pixels is protected and the image quality is preserved. SUVI's CCD does not have sufficient dynamic range to capture both faint features like coronal holes and bright sources like flares in a single exposure. This aspect of the SUVI instrument is addressed by the imaging sequence and the operational scientific products, which are discussed later.

### 1.2.2. Ground Calibration

The initial calibration of each individual SUVI instrument was determined by measuring the response of individual components in the optical path: entrance filters, primary and secondary mirrors, focal-plane filters, and the detector and associated electronics. To demonstrate that SUVI met the performance requirements, the calibrated response of the components were assembled into an instrument model. This instrument model demonstrated not only that spectral response requirements were met, but also that requirements constraining the instrument point-spread function were met. Below we discuss the performance of some key instrument components.

#### 1.2.2.1. Filter Transmission Measurements

A set of SUVI filter witness samples were sent to the National Institute of Standards and Technology (NIST) Gaithersburg Synchrotron Ultraviolet Radiation Facility (SURF-III) for transmission measurements (Arp et al., 2002). The method of measurement was through an insertion technique with a photodiode measuring current. The transmission coefficients were determined by comparing the current from a calibrated reference photodiode while unobstructed to that of the current while the filter was obstructing the beamline. Measurements were repeated until the relative measurement uncertainty fell below 0.25%. The spectral coverage was from 5 to 50 nm, sufficient to cover the entire effective SUVI spectral range.

The measured filter transmission values are then used to create an optical model of the filter properties through the use of optical coefficients from the X-Ray Interactions With Matter on-line database, which is maintained by the Center for X-Ray Optics at Lawrence Berkeley Laboratory ([http://henke.lbl.gov/optical\\_constants/](http://henke.lbl.gov/optical_constants/)). The modeling efforts have been strictly for validation of the vendor-supplied filter thicknesses, as well as to constrain the amount of oxidation and carbon accumulation (Figure 4).

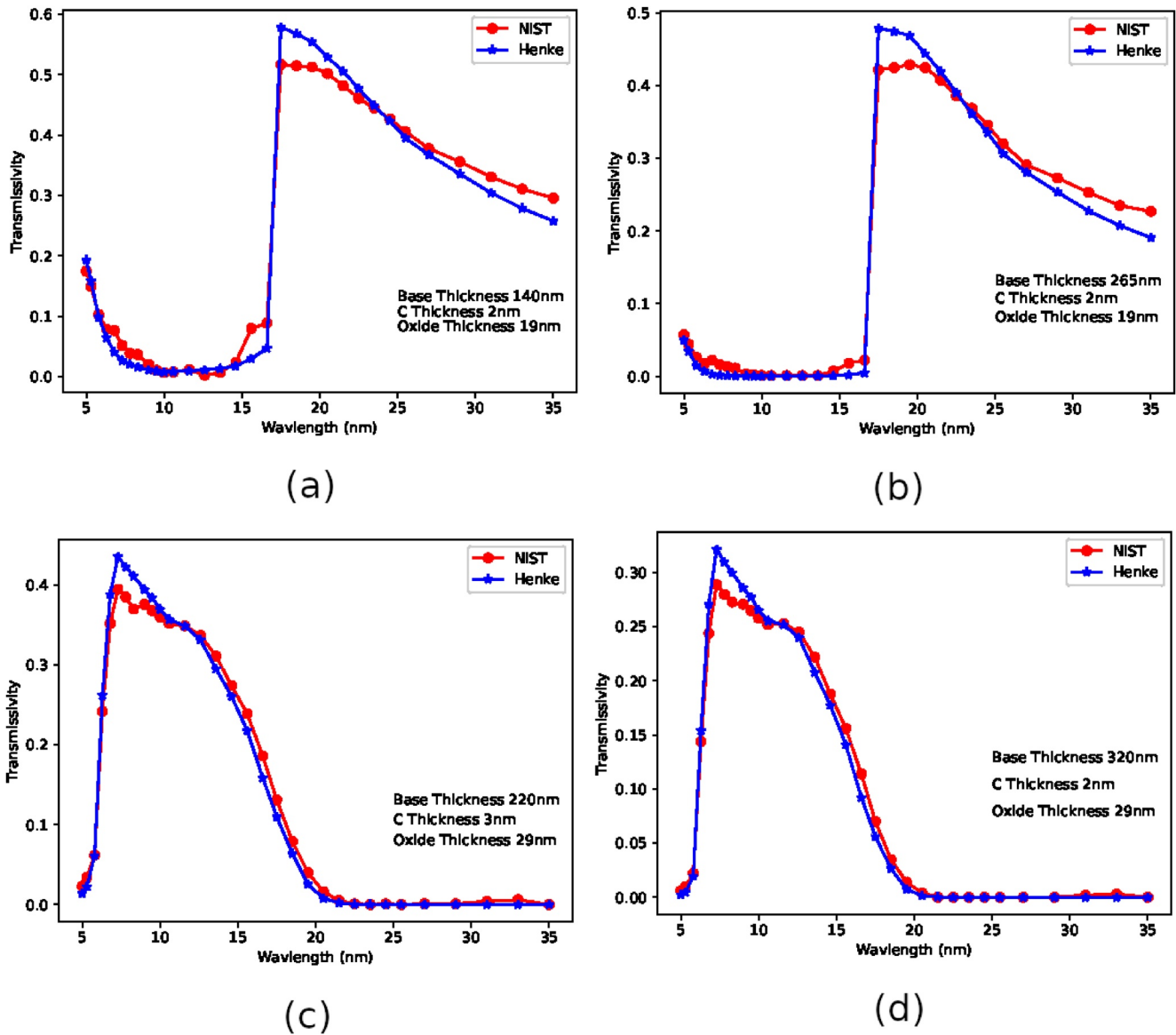


Figure 4. National Institute of Standards and Technology transmission measurements (red) and Henke optical transmission coefficient modeling results (blue).

### 1.2.2.2. Mirror Reflectivity Measurements

The mirror pairs for all SUVI channels utilize constructive interference from multilayer optics to tune the spectral response function of the instrument to achieve the highest possible response at the desired wavelength. The mirror coatings were laid down by Reflective X-ray Optics (94, 195, 284, and 304 Å) and Lawrence Livermore National Laboratory (131 and 171 Å) respectively. Beamline 6.3.2 at the Lawrence Berkeley National Laboratory Advanced Light Source facility was used to inspect and measure the response of each of the mirror coatings. To ensure the uniformity of the mirror response (reflectivity) across each sector of the mirrors, the test measurements were repeated at multiple locations, and the reported reflectivity is a weighted average of those measurements (Figures 5 and 6). The uncertainty of the reflectivity measurements is less than 1% for all channels for all mirror pairs.

### 1.2.2.3. CCD Calibration

The SUVI detectors are all similar CCDs manufactured by Teledyne-e2v (<http://teledyne-e2v.com>). The detectors are all read out at a 1330 × 1292 pixels, reduced to 1280 × 1280 when overscan regions are removed (as in SUVI

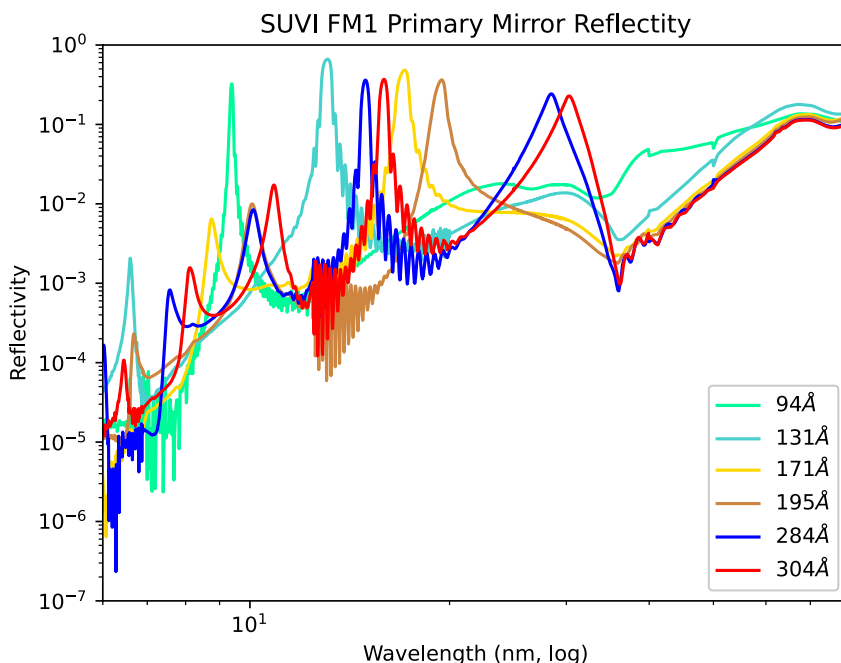


**Figure 5.** Solar UltraViolet Imager (SUVI) FM1 Primary Mirror Reflectivities, all SUVI channels.

Level-1b and derivative products). Detector performance characteristics such as linearity and read noise were determined via light-transfer curves using a white light source. Further ground calibration activities for the SUVI CCDs were conducted in the XUV facility at Lockheed Martin's Solar and Astrophysical Laboratory (LMSAL). These calibration tests determined the detector quantum efficiency and the detector gain.

During all calibration tests, the CCDs were cooled to  $-60^{\circ}\text{C}$ . The low temperature reduced the contribution of dark current to measurement uncertainty to well below 1% for these tests. The long integration times used also reduced the overall contribution to uncertainty from the detector read noise to well below 1%. The system gain of

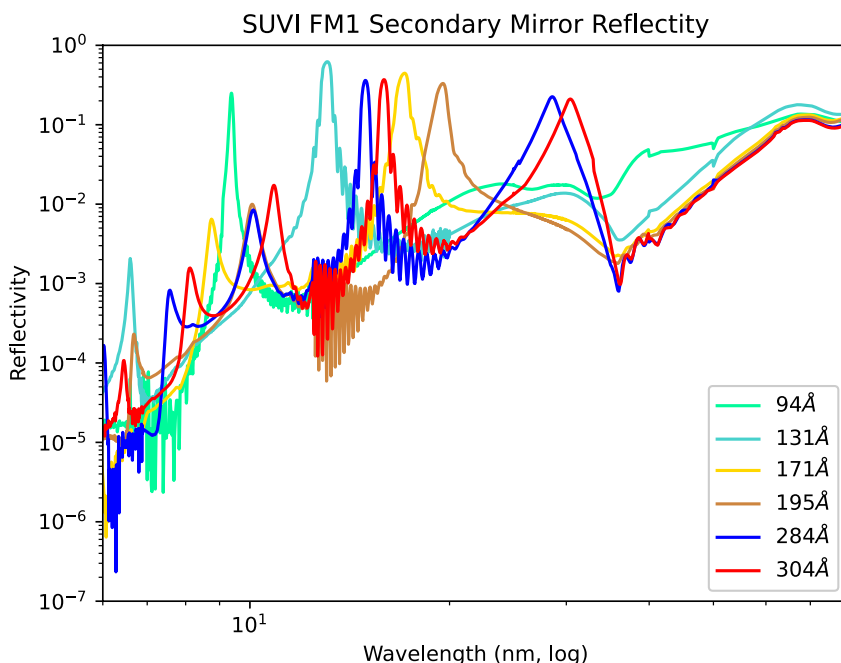


**Figure 6.** Solar UltraViolet Imager (SUVI) FM1 Secondary Mirror Reflectivities, all SUVI channels.

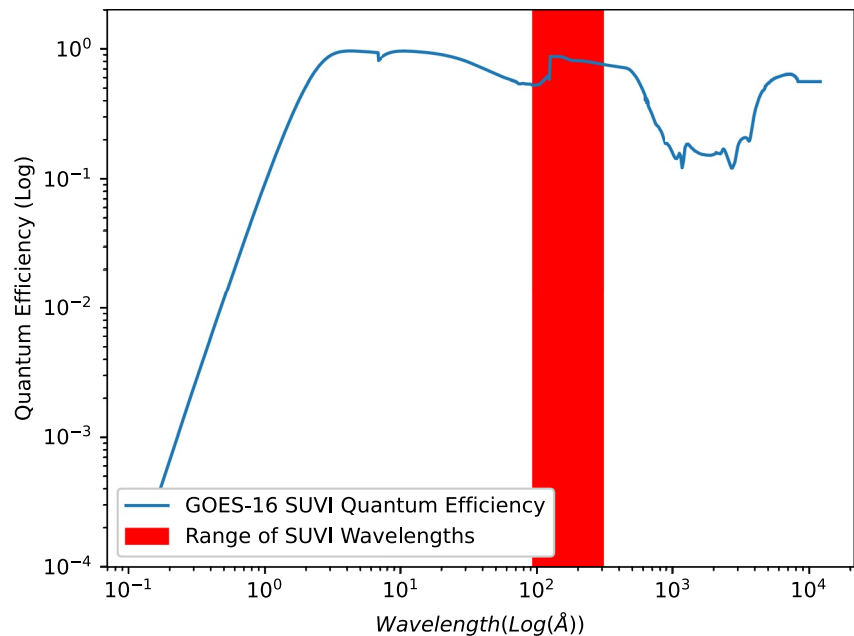


**Figure 7.** Solar UltraViolet Imager (SUVI) Geostationary Operational Environmental Satellite (GOES)-16 charge-coupled device quantum efficiency plotted with the red shaded area showing the SUVI observational range.

the SUVI CCDs were determined by illumination by photons emitted by the decay of  $\text{Fe}^{55}$  atoms over a very long integration time (200 s). To determine quantum efficiency, the SUVI CCDs were illuminated by EUV and X-ray photons at specific wavelengths via a monochromator. Where direct illumination by desired wavelengths were not an option, a proxy wavelength with a similar penetration depth were used. These measurements were then used to fit a semi-empirical detector quantum efficiency model to fill the gaps between measurement points (Figure 7).

This series of tests also characterized the flat field of each CCD, using UV illumination, yielding a measurement of the relative pixel-to-pixel response of the detector. These tests showed that the pixel-to-pixel variation was typically within  $\pm 2\%$ . Pixels whose response deviated beyond 80% relative to the consensus response of the detector were added to the list of known defective pixels. Table 3 reflects the known defective pixels as of the date of publication.

### 1.2.3. On-Orbit

Following delivery to the spacecraft and launch vehicle, the SUVI instruments are kept in a positive pressure, dry-nitrogen purge environment. This minimizes the possibility of contamination accumulating onto optical surfaces or the interior of the instrument. This purge environment is maintained up to and after launch. Once the spacecraft has escaped the Earth's atmosphere, there is an extended phase of decontamination and out-gassing. Survival and decontamination heaters are switched on to prevent the accrual of possible contaminants on optical surfaces. The SUVI front door is also unlatched to encourage the evacuation of contaminants from the instrument.

Once the spacecraft has reached geostationary orbit, but prior to beginning operation, instrument-level testing verifies or validates the calibration of the SUVI instrument that was measured during ground calibration. It is difficult to isolate individual components for testing due to the lack of well-characterized sources that can be incorporated into the instrument design for an instrument operating in the extreme ultraviolet, though multiple combinations of observations can help to isolate the effects of multiple components.

The on-orbit instrument post-launch testing includes mechanical tests for subsystems, such as the aperture selector and filter wheel mechanisms. Mechanical procedures are carried out to open the front door and initialize the filter wheels, shutter, and aperture selector mechanisms. After the

**Table 3**  
*Measured Defective Pixels in Columns on Solar UltraViolet Imager (SUVI) FM1 (Geostationary Operational Environmental Satellite [GOES]-16) and FM2 (GOES-17)*

	Defective pixels	Defective columns	Defective clusters
SUVI FM1 CCD	19	0	1 (cluster of 9 pixels)
SUVI FM2 CCD	0	0	0

*Note.* CCD, charge-coupled device.



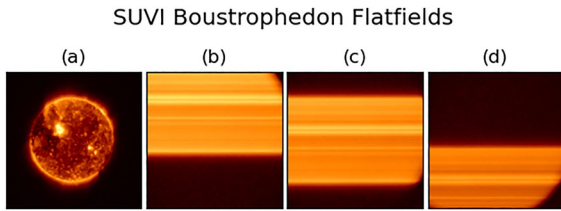


Figure 8. (a) Reference image for 195 Å; (b–d) offset scans.

necessary mechanical tests are complete, the instrument can begin to test and verify the performance characteristics of the optical system. These instrument performance tests characterize aspects of the CCDs, filters, or overall optical system. The CCD is then slowly cooled to an operational temperature, typically around  $-60^{\circ}\text{C}$ . The function of dark current with respect to detector temperature is characterized during this cooling phase. The detector temperature is stabilized at pre-determined set points and sufficient dark exposures are taken to characterize the dark current at that temperature. When the SUVI instrument has reached the operational configuration, further tests to characterize the optimal focus position and determine flatfields are performed.

In-band flatfields are obtained via a series of *Boustrophedon* maneuvers (Dalrymple et al., 2003). These maneuvers utilize the irradiance from the Sun to produce regions of uniform signal on the detector by scanning the Sun across the SUVI detector. The solar array of the GOES-R spacecraft is turned at a steady and slow rate so that the SUVI field-of-view is panned across the Sun. The SUVI takes a single exposure during this time. The effect produces rows of consistent signal across the SUVI detector. Various vertical offsets are applied, and the resulting images can be combined to produce an effective in-band flatfield (see Figures 8 and 9).

## 2. Instrument Performance

### 2.1. Spectral Characteristics

SUVI's design is primarily driven by NOAA's operational needs, creating several key differences between SUVI and other solar EUV telescopes. To demonstrate the differences in performance between SUVI and AIA, we perform a spectral characteristic analysis similar to that described by O'Dwyer et al. (2010) for AIA.

We use CHIANTI (Landi et al., 2013) and ChiantiPy (Dere et al., 2019) with the differential emission measure (DEM) provided in the CHIANTI database for coronal hole, quiet Sun, active region, and flare. We use a uniform electron density,  $N_e = 10^9 \text{ cm}^3$ , and the solar coronal abundances of derived by Schmelz et al. (2012). A similar approach was used to create the temperature response functions seen in Figure 1. The results are folded into the SUVI spectral response functions (Figure 10) and the spectral data are evaluated for the respective contributions.

The results of the analysis are shown in Table 4. For each channel, the ions that contribute the most prominent emission are tabulated along with their fractional contribution for each of the categories of solar features (coronal holes, quiet corona, active region, and flare). Also included is the ratio of the irradiance when compared against that of an active region.

Many SUVI channels behave similarly to their counterparts on AIA, and depending on the goal of the study, the investigator will be justified in treating them so. In some channels, however, the spectral response behavior is sufficiently different that the investigator ought to be mindful in how they interpret the data. This is especially true of the differences between the SUVI 195 Å channel and the SDO/AIA 193 Å channel. Table 4, when contrasted with Table 1 in Schmelz et al. (2012), clearly demonstrates that AIA and the SUVI instruments are observing different solar corona phenomena for those respective channels. Other channels, such as SUVI's 131 Å channel capture many of the same features, but because of differences in the passband, measure significantly different fractional contributions from specific ions.

### 2.2. Spatial Characteristics—Point Spread Function

The spreading of light due to the imperfections in an optical system is described by the point-spread function (PSF). In an ideal scenario, the PSF of the optical system is known or precisely measured, and the deconvolution of the data with this known PSF can be used to minimize the effects of stray light in the science data. Unfortunately this ideal scenario is almost never the

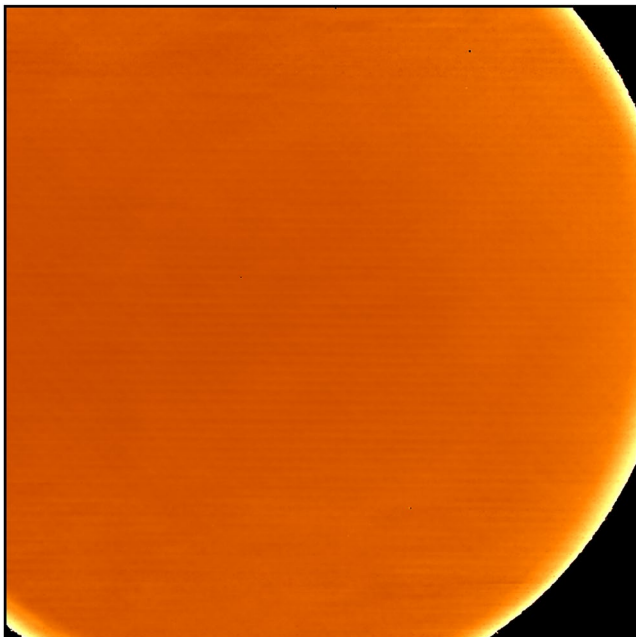


Figure 9. A Solar UltraViolet Imager (SUVI) flatfield created with the Boustrophedon method.

**Table 4**  
*Solar UltraViolet Imager Spectral Features*

	Ion	$T_p^a$ K	Fraction of emission			
			CH	QC	AR	FL
94 Å	Fe VIII	5.6	0.52	0.22	0.09	–
	Fe IX	5.9	0.18	0.19	0.11	–
	Fe X	6.1	0.13	0.32	0.25	–
	Fe XIV	6.3	–	0.07	0.14	–
	Fe XVIII	6.9	–	–	0.24	0.89
	Fe XX	7.0	–	–	–	0.08
	Mg VIII	5.9	0.03	0.03	–	–
	$I^*/I_{AR}$	–	0.01	0.06	1.0	673.7
131 Å	Fe VIII	5.6	0.83	0.83	0.78	0.06
	Fe IX	5.9	–	–	0.01	–
	Fe X	6.1	–	0.02	0.05	–
	Fe XI	6.2	–	0.01	0.02	–
	Fe XX	7.0	–	–	–	0.14
	Fe XXI	7.1	–	–	–	0.45
	Fe XXIII	7.2	–	–	–	0.31
	Mg V	5.6	0.03	0.02	0.01	–
	Ne VI	5.7	0.04	0.03	0.02	–
	O VI	5.5	0.04	0.04	0.04	–
$I^*/I_{AR}$	–	0.08	0.15	1.0	678.8	
171 Å	Fe VIII	5.6	0.02	0.01	–	0.01
	Fe IX	5.9	0.89	0.91	0.89	0.75
	Fe X	6.1	0.02	0.05	0.06	0.03
	Mg IV	5.2	0.01	–	–	0.04
	Ni XIV	6.4	–	–	0.01	0.01
	O V	5.4	0.03	0.01	–	0.08
	O VI	5.5	0.03	0.01	0.01	0.04
	$I^*/I_{AR}$	–	0.03	0.11	1.0	23.1
195 Å	Fe VIII	5.6	0.54	0.19	0.08	0.12
	Fe IX	5.9	0.15	0.12	0.08	0.03
	Fe X	6.1	0.03	0.06	0.06	–
	Fe XI	6.2	0.02	0.12	0.13	0.03
	Fe XII	6.2	0.02	0.41	0.58	0.16
	Fe XIII	6.2	–	0.02	0.03	–
	Fe XXIV	7.2	–	–	–	0.34
	O IV	5.3	0.08	0.02	–	0.09
	O V	5.4	0.14	0.04	–	0.10
	Ca XVII	6.9	–	–	–	0.06
$I^*/I_{AR}$	–	0.01	0.07	1.0	43.3	

case, and we have to determine the shape of the instrument PSF. Those determinations can be made using iterative processes, beginning with an initial guess based either on prior knowledge about the optical setup of the instrument (“semi-blind deconvolution”), or without (“blind deconvolution”).

For GOES-16 SUVI, a PSF model was developed before flight by Martínez-Galarce et al. (2010), but no direct measurements were made. Here, we use a simpler approach for constructing the PSF than those authors employed, as not all components in the SUVI optical path need to be considered. The optical components that could potentially influence the shape of the PSF for SUVI are:

1. Entrance filter
2. Primary mirror
3. Secondary mirror
4. First focal plane filter
5. Second focal plane filter
6. CCD

The entrance filter and the focal plane filters are stabilized by a metal mesh, which can cause a diffraction pattern in the images that is primarily seen during flares and in high-contrast areas. The primary and secondary mirror can influence the shape of the PSF with optical aberrations, and with a diffuse component due to the micro-roughness of the mirror surfaces. Finally, the CCD could potentially contribute to the the PSF with an effect called “charge spreading” when electrons in a pixel can leak into adjacent pixels.

Pre-launch testing of the SUVI CCDs demonstrated that charge-spreading contributes insignificantly outside of the central and immediate neighbor pixels, and is negligible when compared to the effects of the optical PSF. We may therefore ignore the effect of charge spreading for our PSF model. Also not considered are the two focal plane filters, as no “double-cross” diffraction pattern can be seen in SUVI images during flares, only a single cross originating from the entrance filter mesh. This is expected: due to the proximity of the focal plane filters and the CCD in the optical path, the diffraction pattern from the focal plane filters should not create a visible contribution in the images. Lastly, the primary and secondary mirror are being treated as one optical component for our PSF model.

While first results with our model are encouraging (see Figure 11 for PSF deconvolution examples in 171 and 304 Å), finding appropriate point spread functions for each channel remains ongoing research. More work needs to be done to ensure the deconvolution process does not remove scientifically valuable data from the images, particularly in low signal-to-noise regions in the outer corona. Details of the PSFs for GOES-16 and GOES-17 for all wavelength channels will be discussed in a subsequent paper.

### 2.3. Instrument Degradation

The optical throughput of space-based instruments degrades over time due to radiation-induced aging and the polymerization of contaminants on optical surfaces in the instrument. Degradation in modern solar EUV instrumentation is thought to be dominated by the oxidation of the entrance filter and accumulation of hydrocarbons and other contaminants (e.g., Berthelot & Gaudenchon, 1910) onto surfaces in the optical system, which can be partially mitigated through contamination control plans (Tarrío et al., 2021).

**Table 4**  
*Continued*

	Ion	$T_p^a$ K	Fraction of emission			
			CH	QC	AR	FL
284 Å	He II	4.9	0.54	0.33	0.08	0.62
	Fe VI	5.2	0.05	0.03	–	0.04
	Fe XIV	6.3	–	–	0.06	–
	Fe XV	6.4	–	0.15	0.53	0.13
	Mg VII	5.8	0.08	0.07	0.03	–
	O IV	5.3	0.10	0.06	–	0.08
	Si VII	5.8	0.09	0.08	0.04	0.01
	Si IX	6.1	–	0.04	0.04	–
	$I^*/I_{AR}$	–	0.03	0.07	1.0	152.3
304 Å	He II	4.9	0.95	0.87	0.65	0.95
	O III	5.1	0.02	0.02	0.01	0.02
	Si IX	6.1	–	0.01	0.03	–
	Si XI	6.2	–	0.03	0.15	–
	$I^*/I_{AR}$	–	0.15	0.22	1.0	780.4

*Note.* The spectral contributors to each SUVI channel as categorized by solar feature (coronal hole [CH], quiet coronal [Qc], active region [AR], and flare [FL]). The temperature of peak emission for each emission line is provided ( $T_p^a$ ), as well as the ratio against the irradiance from an active region ( $I^*/I_{AR}$ ).

Various methods have been used to correct for degradation in solar EUV imagers (e.g., BenMoussa et al., 2013; Boerner et al., 2014), and typically require a calibrated absolute reference against which to compare the disk-integrated image signal over time. For AIA, the degradation factors (available through the SunPy and SolarSoft packages.) were found using calibrated high spectral resolution EUV irradiance measurements from the EUV Variability Experiment (EVE; Woods et al., 2012) onboard SDO prior to the short wavelength spectrograph failure in 2014 and modeled EUV irradiance measurements from the Flare Irradiance Spectral Model (FISM; Chamberlin et al., 2007) after 2014 (Boerner et al., 2014). There are currently no calibrated absolute EUV irradiance references that can be used to accurately derive the degradation for arbitrary narrowband channels in imagers like SUVI. Irradiance measurements from the Extreme Ultra-Violet Sensor (EUVS; Eparvier et al., 2009) onboard GOES provide calibrated and degradation-corrected irradiance measurements, however these observations only overlap two SUVI channels (284 and 304 Å) leaving four channels (94, 131, 171, and 195 Å) without a calibrated irradiance reference. Given the overlap between the SUVI and AIA 94, 131, 171, 195, and 304 Å channels, we estimate the degradation in the remaining channels using degradation-corrected AIA images that have been tuned to EVE observations.

For GOES-16, we use operational SUVI data from May 2018 to present and reprocessed data prior to May 2018 (due to numerous anomalies in the early operational data), while operational SUVI data is used for the full GOES-17 mission. We omit the GOES-17 SUVI 94 Å channel from this analysis due to a pinhole in the entrance filter for this channel causing a significant visible light leak. Figure 12 shows the current mission-length disk-integrated

response of the GOES-16 and -17 SUVI channels without any degradation correction and normalized to the integrated response at the start of the mission. The SUVI responses are dominated by the solar cycle signal, however degradation is apparent in the 304 Å channel, particularly in the GOES-16 plots. The noise in the GOES-16 SUVI 94 Å channel largely results from contamination by low-energy electron spikes on the detector, which overwhelm the low irradiance of this channel. Due to problems in the data production pipeline early in the mission, fully removing the effects of energetic particle hits without a significant reprocessing effort is difficult. Although such reprocessing is underway, these data are not available at the time of writing.

We estimate the degradation by computing the ratio of the disk-integrated SUVI channel responses for GOES-16 and -17 shown in Figure 12 to the respective irradiance reference measurements for a given channel, normalizing to the ratio at the mission start. We use the science-quality EUVS irradiances as the reference measurements for the 284 and 304 Å channels and degradation-corrected AIA measurements for the 94, 131, 171, 195, and 304 Å channels. The results are shown in Figure 13 and summarized in Table 5. The GOES-16 SUVI 94 Å channel degradation estimate is overwhelmed by noise due to the particle contamination.

For the remaining channels, we estimate less than 40% total degradation over the two missions. Importantly, the degradation experienced by both SUVI instruments is considerably less than that experienced by AIA (Boerner et al., 2014). For example, in the 304 Å channel, AIA experienced approximately 90% degradation in the first five years of operations while we estimate that GOES-16 SUVI experienced between 25% and 40% degradation in this same time period. The difference in degradation rates is likely due to improved cleanliness practices and the choice of a less-volatile thruster propellant for the GOES spacecraft than the propellant used by the SDO spacecraft. These results provide initial estimates of the SUVI degradation. A full degradation analysis is the topic for a future paper, after which the time-dependent degradation corrections will be provided for SUVI data users.

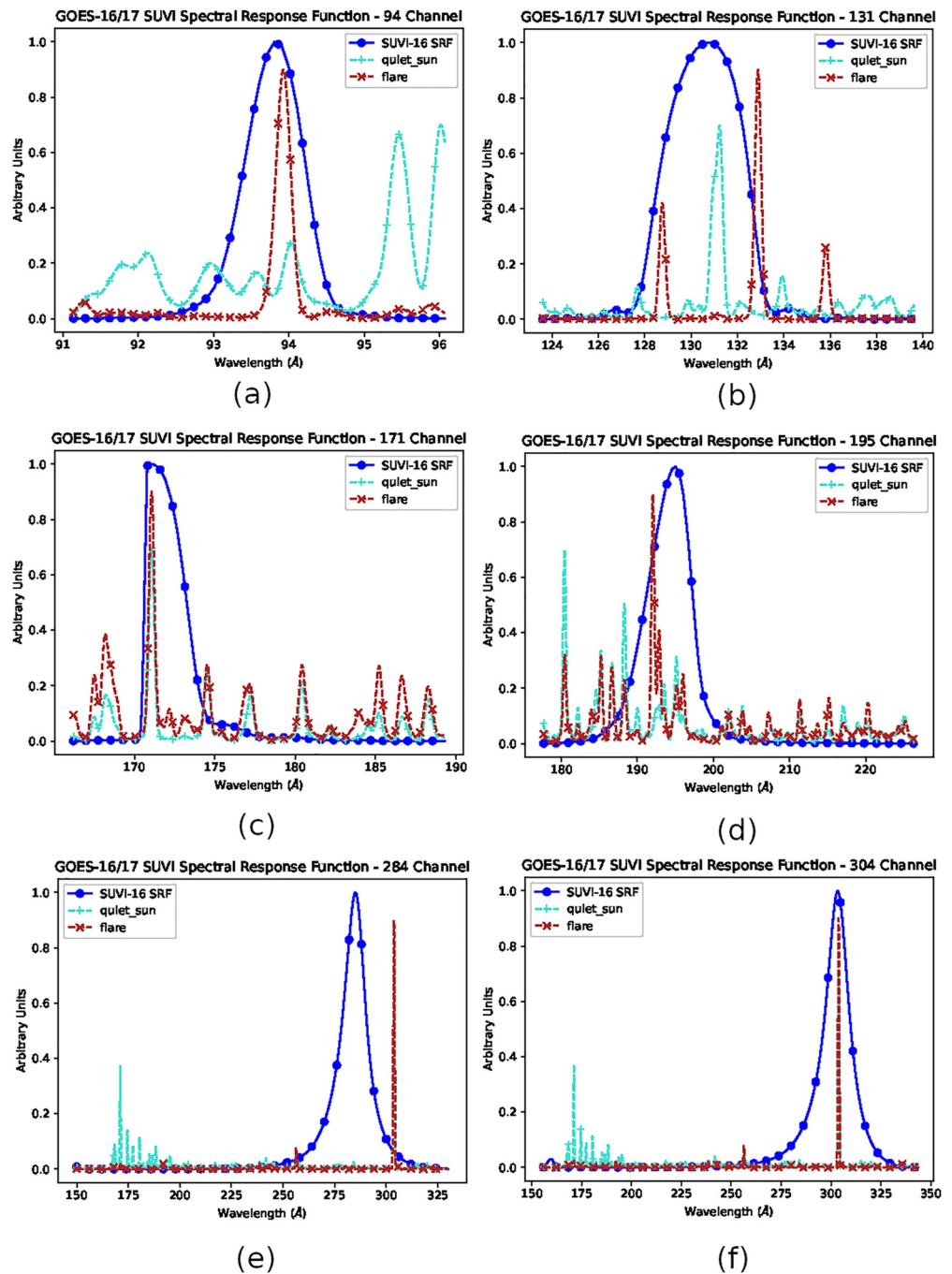


**Figure 10.** Solar UltraViolet Imager spectral response functions for each channel (blue, normalized) shown with quiet coronal spectra (teal) and flaring spectra (red).

### 3. SUVI Products

The primary publicly available SUVI data product are the calibrated Level-1b files, available as either FITS or netCDF formatted files. Level-0 (or “raw”) data is generally not available as the Level-0 data exists primarily as packetized data. Level-2 SUVI products are created and available through SWPC as forecast products in PNG format with latency less than 5 minutes, or from the National Centers for Environmental Information (NCEI) as science products with a latency of a few hours. A detailed discussion of SUVI observations and data products

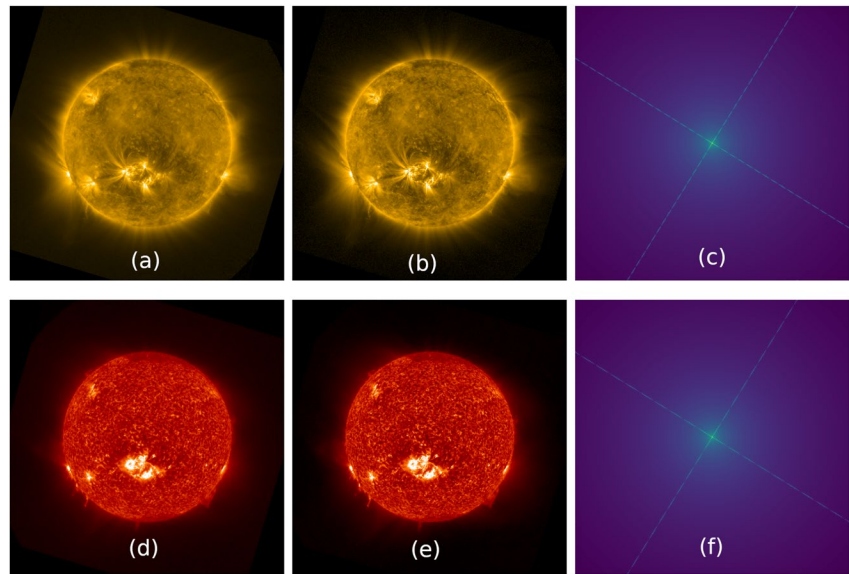


**Figure 11.** Illustration of image deconvolution using the point spread function (PSF) in the Geostationary Operational Environmental Satellite (GOES)-16/Solar UltraViolet Imager (SUVI) 171 Å and 304 Å channels during an M4.4 flare on 29 November 2020. (a) 171 Å (b) 171 Å deconvolved, (c) preliminary PSF for 171 Å (d) 304 Å (e) 304 Å deconvolved, (f) preliminary PSF for 304 Å.

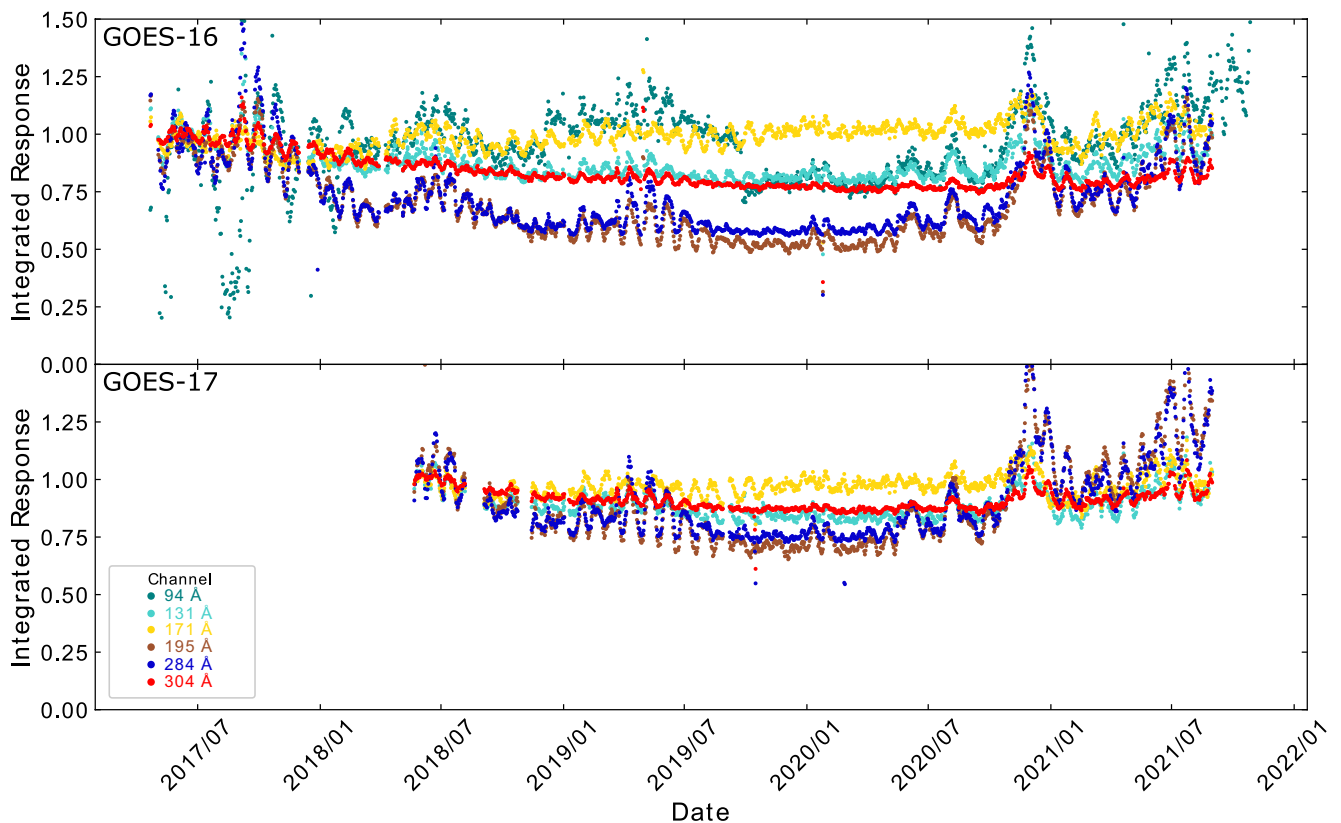


**Figure 12.** Geostationary Operational Environmental Satellite (GOES)-16 (top) and GOES-17 (bottom) Solar UltraViolet Imager (SUVI) disk-integrated channel responses over the current mission lifetime without degradation correction normalized to the mission start response. The GOES-17 94 Å channel is omitted due to visible light contamination resulting from an entrance filter light leak.

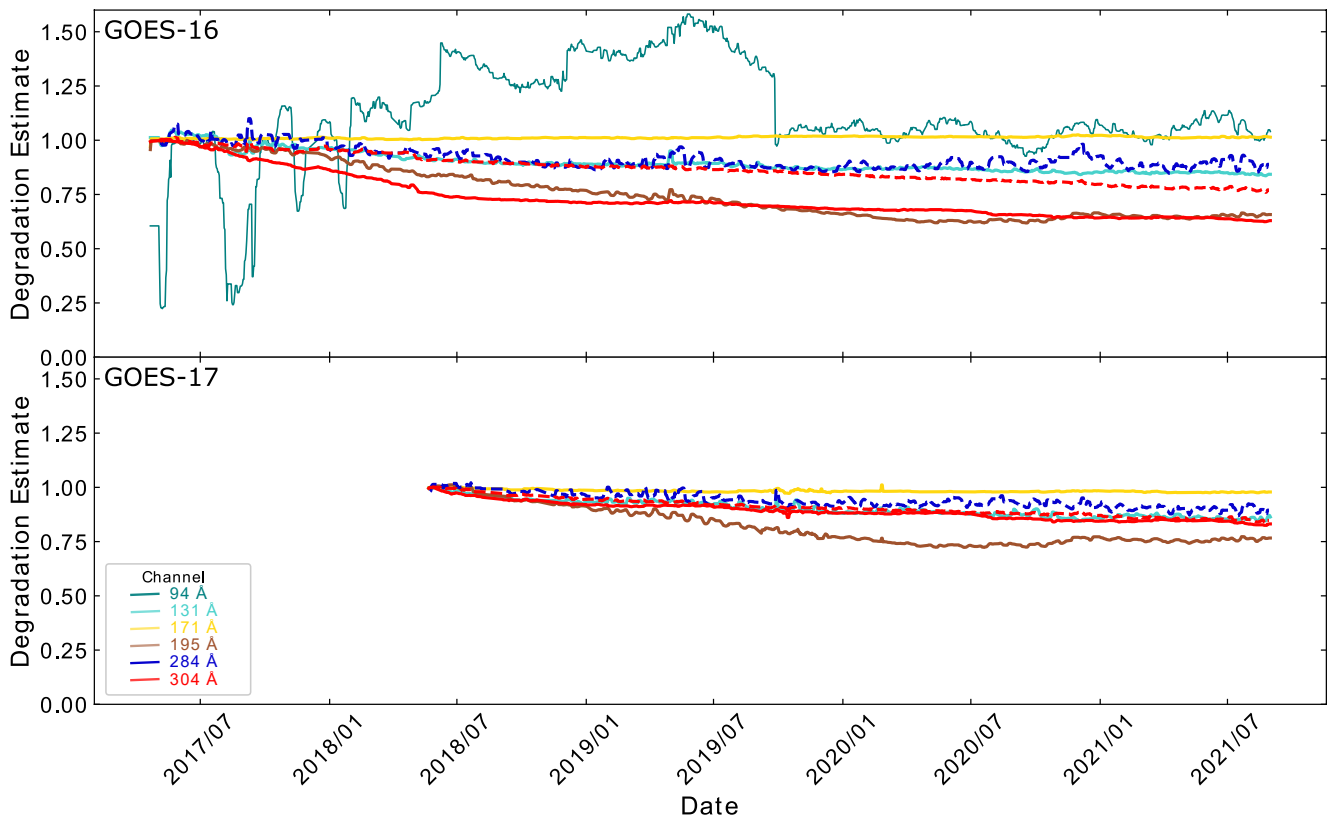


**Figure 13.** Estimated Atmospheric Imaging Assembly (AIA)- and Extreme UltraViolet Sensor (EUVS)-derived degradation trends for all SUVI channels for the instruments onboard GOES-16 (top) and GOES-17 (bottom) using AIA measurements (solid lines) or EUVS measurements (dashed lines) as the calibrated reference. The GOES-17 SUVI 94 Å channel is omitted due to visible light contamination. The data have been smoothed with a 10-day running average window to highlight the trends.

appears in (Seaton et al., 2020). Figure 14 shows an overview of different SUVI data products and the flow from data level to data level.

Level-0 observations are uncalibrated camera frames while L1b files are calibrated individual observations in radiometric units. L2 image-based products include *composite high dynamic range (HDR) images*, generated from multiple SUVI observations; *thematic maps*, which are pixel-by-pixel maps of specific features of interest for space weather forecasting; and *coronal hole images* which are low-noise long-exposure composite images that highlight the dimmest features in SUVI observations. Several reports are also derived from these products, including reports that track active regions, flare locations, and coronal holes that are available through NCEI (<https://www.ngdc.noaa.gov/stp/satellite/goes-r.html>).

**Table 5**  
*Mission-Length Degradation Estimate for Geostationary Operational Environmental Satellite (GOES)-16 and -17 Solar UltraViolet Imager (SUVI) Instruments for All Channels Excluding 94 Å*

Channel (Å)	Calibrated reference	Degradation estimate	
		GOES-16 SUVI	GOES-17 SUVI
131	AIA	16%	14%
171	AIA	0%	2%
195	AIA	34%	23%
284	EUVS	11%	10%
304	AIA	37%	17%
	EUVS	23%	15%

*Note.* AIA, Atmospheric Imaging Assembly; EUVS, Extreme UltraViolet Sensor.

### 3.1. The SUVI Level-1b Product

As discussed in Section 1.1, SUVI uses a repeating sequence of long ( $\approx 1$  s), short ( $\approx 5$  ms), and, in some cases, short flare ( $\approx 5$  ms with extra focal plane filters to further attenuate signal) in each of its six passbands to ensure that every pixel in the field of view is both adequately exposed, but also unsaturated in at least one image per sequence. Each individual image obtained at the spacecraft is calibrated within the GOES-R ground segment and converted into a L1b image, in camera coordinates, rectified so solar north on the top side of the image, and reported in standard units of radiance ( $\text{W m}^{-2} \text{sr}^{-1}$ ).

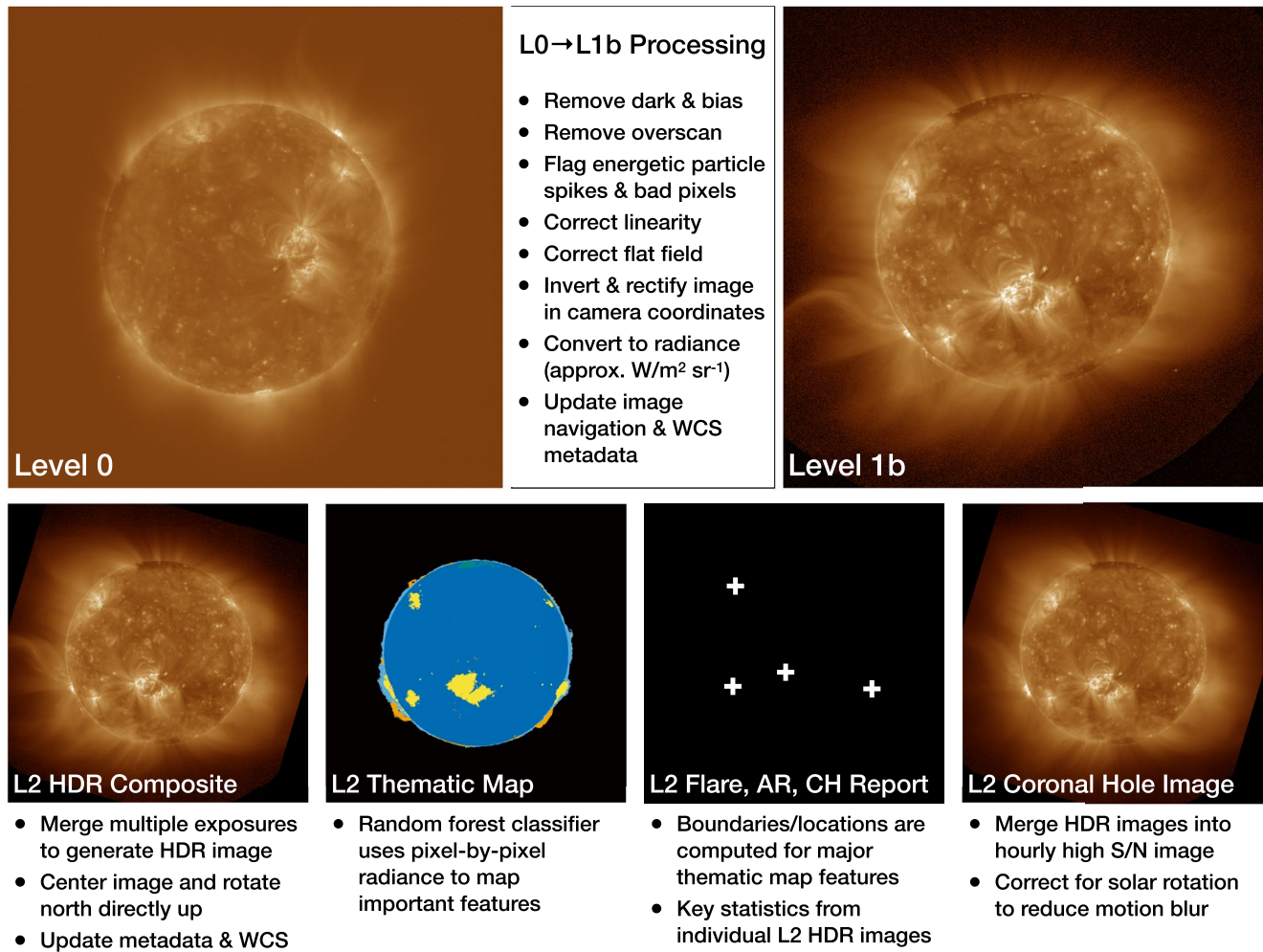


**Figure 14.** Overview of Solar UltraViolet Imager (SUVI) data levels and the processing steps to generate each product. Additional details about specific products appears in Sections 3.1 and 3.2. Note that L2 Flare Summary, Bright Region, and Coronal Hole products are not image products.

Table 6 provides an overview of the standard SUVI observing sequence at the time of writing. Adaptations to adjust for instrumental degradation or performance are expected to occur at a future date.

Each type of exposure uses a different combination of mirrors, filters, and exposure, and receives a unique label, or “science objective,” to help quickly identify them during image processing. L1b files also include a secondary array, the “data quality flag” that indicates the location of missing data, bad camera pixels, spikes resulting from energetic particle hits. Where possible, these defects are removed during Level-2 processing. L1b files are primarily delivered in FITS format, familiar to most astronomical data users, but are also available as netCDF files, which are more commonly used in the atmospheric science and weather forecasting communities—and are the primary standard for other GOES-R observations. Additional details about SUVI L1b data and data access are available via <https://doi.org/10.7289/V5FT8J93>.

### 3.2. SUVI Level-2 Products

Several higher level products are created from the L1b calibrated images, which will each be discussed below. First, *High Dynamic Range Images* are created from the L1b images. These are then combined into *Thematic Maps*, which are created by a machine learning algorithm that partitions the sun into physical regimes: on-disk quiet Sun, limb (off disk quiet-Sun), bright region (such as in an active region), filament, prominence, coronal hole, and flare. Further products are then created from the Thematic Map: *Coronal Hole*

*Boundaries, Bright Region Summaries, and Flare Summaries* Further details on SUVI L2 products are available via <https://doi.org/10.25921/D60Q-G238>.

### 3.2.1. High Dynamic Range (HDR) Images

HDR images are created for each channel by combining multiple short and long exposure images into a single unsaturated image that maximizes image signal-to-noise ratio everywhere (Figure 15). HDR images are produced from all of the images in a channel that were taken during a single 4-min sequence, which varies between two and seven images per channel as dictated by the sequence. The number of images used for each HDR image is tracked in the HDR metadata. Special coronal hole HDR images are also created from 60 min of data to maximize signal-to-noise in the dim coronal hole (and off-limb) regions of the solar disk. Each pixel ( $p_i$ ) in an HDR image is calculated as a weighted average of all of the corresponding pixels in the  $N$  frames to be averaged. In most pixels—including coronal holes, quiet Sun, and off disk—the long exposures have better S/N so the corresponding HDR pixel is the average of just the corresponding long exposure pixels. HDR pixels that near saturation in the long exposure image, for example, in bright active regions or flares, use an average of pixel intensities heavily weighted to favor the pixel intensities from the short exposure frames. In this way all of the pixels in the HDR images are unsaturated and have the highest possible S/N. The HDR images are the primary product for SWPC forecaster situational awareness.

### 3.2.2. Thematic Maps

Thematic maps are images where each pixel in the SUVI field-of-view is classified into different categories called themes, that is, coronal hole, quiet Sun, bright region, flare, prominence, filament, and limb. Each pixel is assigned exactly one theme using a random forest, a supervised machine learning algorithm described below. These are produced every 4 min as a FITS file.

The algorithm currently used to produce operational thematic maps is an improved version of the random forest approach described in Hughes et al. (2019). The current algorithm is still a pixel based random-forest approach, that is, it classifies each pixel separately with a random forest without knowledge of neighboring pixels and instead only using spectral information from the six SUVI channels. The random forest operates on the image divided into three circular zones extending radially outward from the center of the image, which represents pixels on the solar disk, off-disk, and in far outer space. By dividing the classification radially, we allow the random forest to understand a rough sense of pixel position. A separate random forest model is trained in each of these layers for every theme that can physically be present in that layer. For example, the on-disk layer classifies only coronal hole, bright region, flare, quiet Sun, and filament and disregards themes such as prominence that do not occur on-disk. During image classification, the output from these theme-dependent random forest models

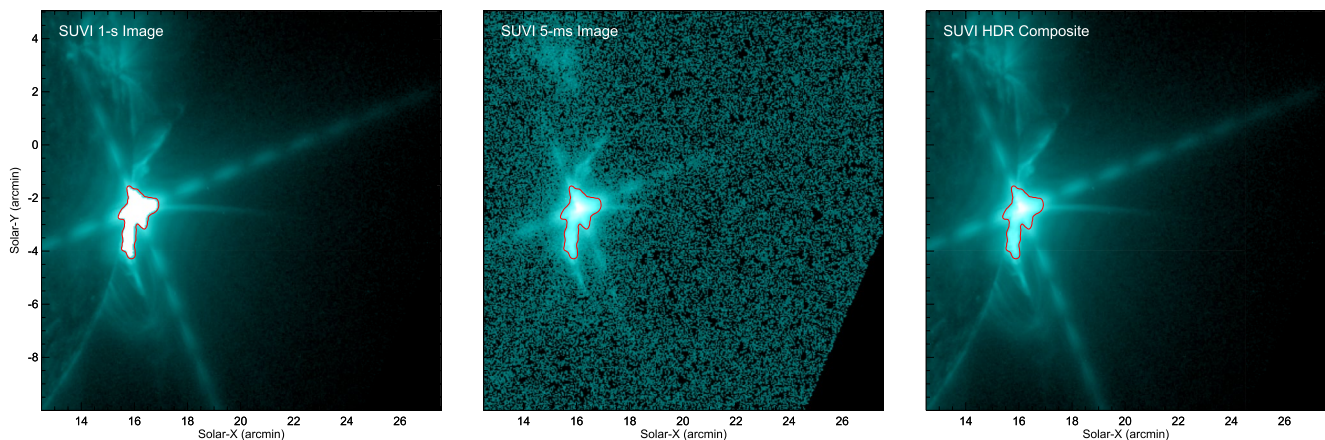


**Figure 15.** Solar UltraViolet Imager (SUVI) 131 Å images from Geostationary Operational Environmental Satellite (GOES)-16: (left) A 1 s long exposure SUVI L1b image of a flaring region, where the central flaring area inside the solid line is saturated; (middle) A 5 ms short exposure SUVI L1b image with no saturation, but many of the pixels outside of the flaring region are very low S/N; (right) An high dynamic range composite image made up of 4 min of data, 4 total individual exposures, which combined long and short exposure L1b images into a single frame that is high S/N and does not contain any saturated images. The pixels inside the solid line are averages of short exposure L1b images, and the pixels outside the solid line are averages of long exposure L1b images.



**Table 6**

*Solar UltraViolet Imager L1b Data Product Names, Filter Combinations, and Exposure Times for Each Wavelength Channel*

L1b data product name [SCI_OBJ]	Filter wheel 1 [FILTER1]	Filter wheel 2 [FILTER2]	Exposure time [s] [EXPTIME]	Wavelength channel [WAVLNTH]
Fe_XVIII_93.9A_short_flare_exposure	thin_zirconium	thin_zirconium	0.005	94
Fe_XVIII_93.9A_short_exposure	thin_zirconium	open	0.005	
Fe_XVIII_93.9A_long_exposure	thin_zirconium	open	1	
Fe_VIII_131.2A_short_flare_exposure	thin_zirconium	thin_zirconium	0.005	131
Fe_VIII_131.2A_short_exposure	thin_zirconium	open	0.005	
Fe_VIII_131.2A_long_exposure	thin_zirconium	open	1	
Fe_IX_171.1A_short_flare_exposure	thin_aluminum	thin_aluminum	0.005	171
Fe_IX_171.1A_long_exposure	thin_aluminum	open	1	
Fe_XII_195.1A_short_flare_exposure	thin_aluminum	thin_aluminum	0.005	195
Fe_XII_195.1A_long_exposure	thin_aluminum	open	1	
Fe_XV_284.2A_short_flare_exposure	thin_aluminum	thin_aluminum	0.005	284
Fe_XV_284.2A_long_exposure	thin_aluminum	open	1	
He_II_303.8A_short_flare_exposure	thin_aluminum	thin_aluminum	0.005	304
He_II_303.8A_long_exposure	thin_aluminum	open	1	

*Note.* The keywords in small caps and square brackets denote the according fits header keyword/variable name in the L1b fits/netCDF files.

yields a probability that each pixel in a given layer corresponds to that theme. Therefore, a confidence threshold can be set to avoid uncertain classifications where a pixel was only slightly likely to be a theme other than quiet Sun. As a consequence, the thematic map classifications erratically fluctuate between themes less often since a classification must have high certainty. Figure 16 shows one example of a thematic map, computed during a moderately sized flare on 29 November 2020.

### 3.2.3. Thematic Map Derived Products

Several Level-2 data products are created from the Thematic Map by extracting information from the map.

The *Coronal Hole Boundary* product takes the identified coronal hole pixels and uses an algorithm to group those pixels into coronal hole regions through dilation and erosion methods. It then draws a simplified boundary around these holes by identifying up to 16 boundary vertices. The product is delivered in netCDF format, where the list of boundary pixel locations is provided for each individually identified coronal hole. These products also provide information about the area and center of each coronal hole.

Similar to the Coronal Hole Boundary product, the *Bright Region Summary* product groups the Bright Region pixels into distinct Bright Region areas. For each identified Bright Region, the netCDF product reports the area, location, and the integrated and peak flux in each of the six SUVI wavelength channels.

If a flare is detected in a Thematic Map, then a netCDF *Flare Summary* product is created. This product includes information on the associated Bright Region and NOAA AR/SS number (<https://www.swpc.noaa.gov/products/solar-region-summary>) if applicable, whether GOES-R EXIS/XRS or EXIS/EUVS also detected a flare, the flare location, and the integrated and peak flux in each of the SUVI wavelength channels.

### 3.3. Coronal Hole Images

Coronal Hole Images are long-duration stacks of L2 HDR composite images (see Section 3.2.1) intended to provide very high signal-to-noise renderings even of very faint structures. Although originally conceived primarily to ensure high-quality observations of coronal holes, these images are also useful for tracking faint structures in the far off-limb region, especially in the middle wavelengths (171, 193) where extended coronal structures are prominent.

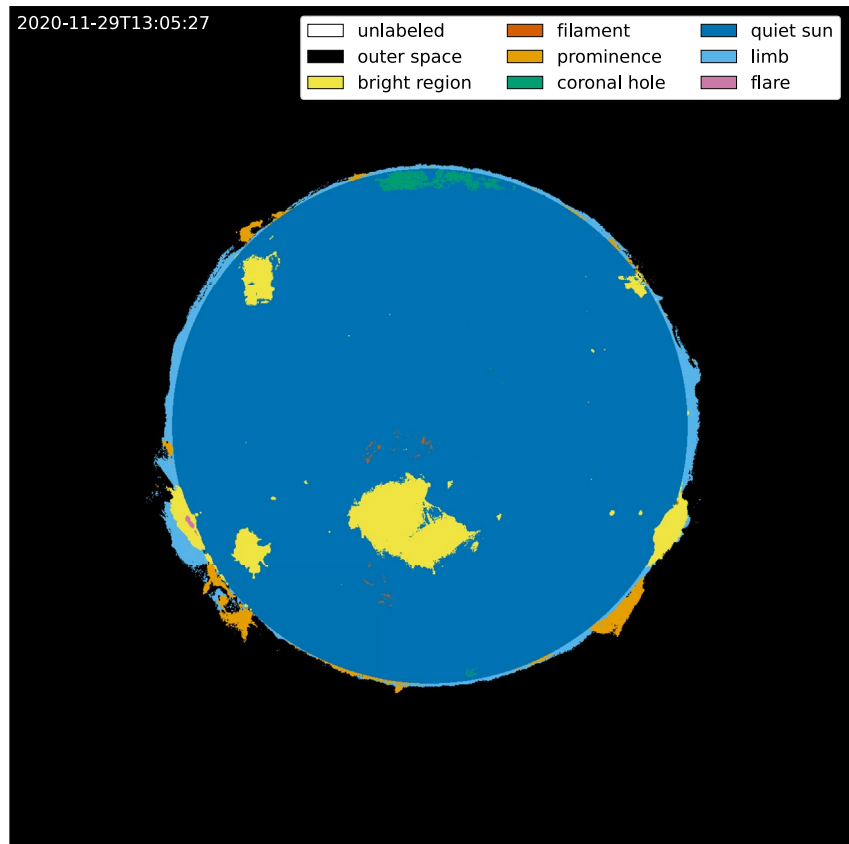


**Figure 16.** Sample thematic map on 29 November 2020 at 13:05:27 UTC.

Operationally, these images are produced at one-hour cadence, meaning each image is typically the summation of 15 individual L2 HDR inputs. This interval is long enough for solar rotation to blur features near the center of the disk. Any correction to the differential solar rotation based on the relative age of each image and solar latitude of the pixel cannot fully account for the optically thin nature of the solar corona and the evolving structures therein. The algorithm applies a best-fit differential rotation correction prior to stacking the images for on-disk pixels.

Note that the differential rotation of off-limb structures cannot be corrected without additional knowledge of their three-dimensional structure. However, this effect is not significant off-limb because the rotation is generally negligible. This is true both at the equator, because the rotation direction is along the line of sight, and at the poles, because the motion of structures is very small over a one-hour period. Off-disk pixels are directly averaged from the input images.

A sample coronal hole image appears in the lower-right panel of Figure 14.

### 3.4. SUVI Software Tools

Software tools, guides, and example code to aid the researcher are available in both the IDL and Python programming languages. For IDL, packages for working with SUVI data are available through the SolarSoft project (Freeland & Handy, 1998). Currently the SUVI package predominantly contains software for reading GOES-16 and GOES-17 SUVI data and recovering the instrument response functions. More will be added as more satellites become operational and more functionality is developed.

Python software for SUVI will be accessible to the community through `sunkit_instruments` (<https://docs.sunpy.org/projects/sunkit-instruments/en/stable/>), a code package affiliated with the SunPy project (The SunPy Community et al., 2020) with the intention to collect solar instrument-specific code under one roof. Additionally, there is a growing collection of GOES Space Weather code examples in the form of Jupyter notebooks on the CIRES-STP GitHub site (<https://cires-stp.github.io/goesr-spwx-examples/examples/index.html>).

Software packages for handling the Level-0 SUVI data have been developed by both LMSAL (under a NASA contract) and NCEI. The LMSAL Level-0 software package utilizes the Level-0 to collect event messages and warnings from the SUVI instrument and trending parameters relevant to mechanism characteristics, thermistor readings, and other relevant performance characteristics ([https://suvi.lmsal.com/doc?cmd=vcur&proj\\_num=SU-VP-RP-19-7061](https://suvi.lmsal.com/doc?cmd=vcur&proj_num=SU-VP-RP-19-7061)). The NCEI Level-0 data software package is utilized to reconstruct raw image files from the Level-0 data and to collect instrument performance characteristics relevant to the instrument calibration.

## 4. Scientific Opportunities With SUVI

Although SUVI has modest temporal and spatial resolution compared to contemporary EUV solar imagers such as AIA, its unique features, capabilities, and products mean that its data are highly complementary, and particularly well-suited to some specific applications. In this section we briefly describe a few of these special capabilities and data sets, and their value for particular problems in solar physics and space weather.

### 4.1. Extended Coronal Imaging

Several recent studies have briefly characterized the EUV corona at heights beyond the fields of view of traditional EUV imagers (e.g., Goryaev et al., 2014; O'Hara et al., 2019; Seaton, De Groof, et al., 2013) and demonstrated the viability of large-field-of-view observations to observe potential space-weather drivers. Since the only available synoptic observations of CMEs from the Earth's perspective are provided by the aging Large Angle and Spectrometric Coronagraph (LASCO; Brueckner et al., 1995) on SOHO, launched in 1995, several recent campaigns explored the potential to use off-pointed SUVI images to serve as a backup for LASCO in the event of a failure or extended outage. At present, LASCO is the only synoptic coronagraph that provides characterizations of CME direction, speed, expansion, and mass from the Earthward perspective—parameters required by forecasters as inputs for models such as WSA-Enlil (Arge & Pizzo, 2000) for predictions of CME arrival times and geoeffectiveness.

A 2018 SUVI Extended Coronal Imaging (ECI) test campaign (Tadikonda et al., 2019) demonstrated a proof-of-concept observation strategy with SUVI, and subsequent campaigns in 2018 and 2019 (Seaton et al., 2021) fully characterized the EUV corona to heights above  $4 R_{\odot}$  over timescales of one to several solar rotations. These campaigns explored different strategies to optimize cadence, resolution, passband, and signal-to-noise in these observations, and ultimately selected a three-panel mosaic approach using SUVI's 171 and 195 Å passbands. The side panels are constructed by median-stacking five 17-s exposures obtained over a period of 100-s, while the central panel, where the EUV signal is much stronger, is a single 10-s exposure. The center points of the side panels are offset by  $47'$  from disk center, yielding a total field of view of  $147' \times 53.3'$ , extending to around  $5 R_{\odot}$  in the horizontal direction. Including observation time for each panel in two passbands and the time required to re-point SUVI between panels, the mosaic observing cadence is approximately 10 min. Although these campaigns conclusively demonstrated that SUVI *can* detect CMEs and other bulk flows in the corona, both occurred during solar minimum conditions, and too few CMEs occurred during these periods to fully characterize SUVI's CME detection capabilities.

A third campaign, executed in conjunction with Parker Solar Probe's Perihelion 8, ran from 27 April 2021 15:00 UT to 30 April 2021 15:00 UT. Figure 17 and the accompanying animation provide an overview of the observations. This campaign produced observations of several CMEs, two of which (on 29 April at 16:15 UT and 30 April at 12:34 UT) were also detected by the Computer Aided CME Tracking (CACTus; Robbrecht et al., 2009) software.

Although they represent only small sample, these several campaigns have demonstrated that, in general, CMEs detected by CACTus are also visible in SUVI ECI observations. These campaigns also demonstrated how CMEs sometimes exhibit strongly non-radial motions in the low and middle corona, so CME initiation is best characterized by overlapping observations in EUV and visible light coronagraphs. Importantly (Bein et al., 2011), found that CMEs that undergo the strongest acceleration, typically experience their peak acceleration at low heights (a few tenths of a solar radius above the solar surface). So, aside from very gradually accelerated events, SUVI detections at the outer edge of the ECI field of view (above  $3R_{\odot}$ ) appear to provide reasonable estimates for final CME velocities in the majority of cases. Additional campaigns planned in 2022, as well as the upcoming

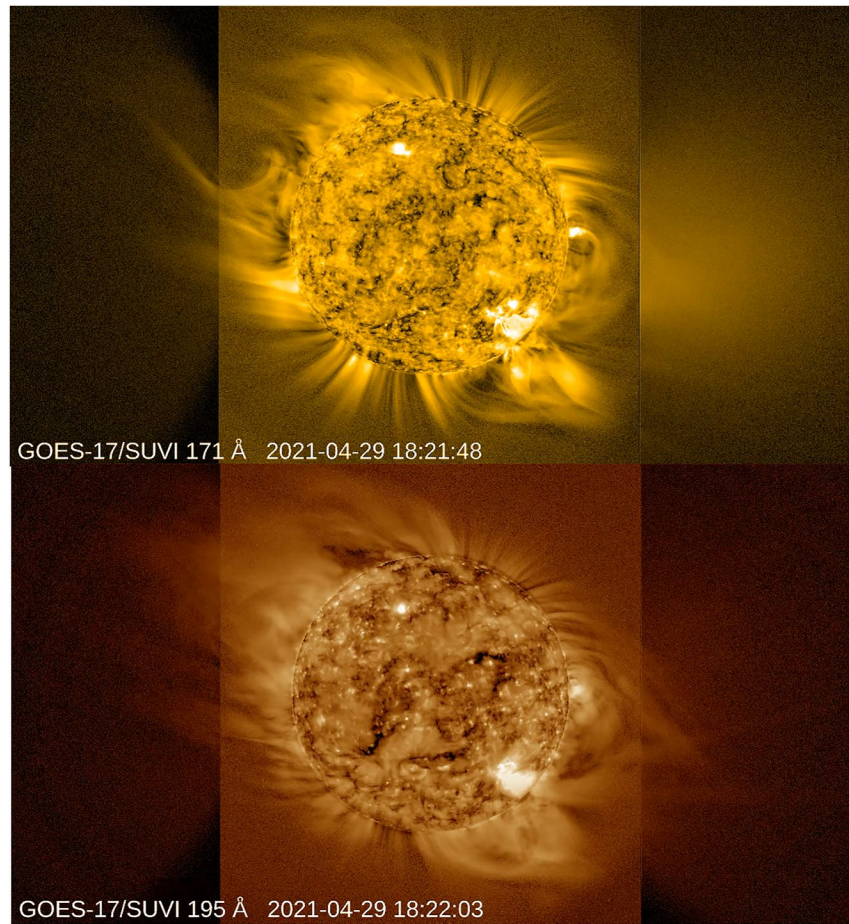


**Figure 17.** Radially filtered mosaic images of the onset of a CME during the 2021 April Solar UltraViolet Imager Extended Coronal Imaging campaign in 171 Å and 195 Å passbands. The mosaic images are cropped at about  $3 R_{\odot}$ . Note that solar north is rotated  $\approx 24^{\circ}$  clockwise from vertical. (Animations of both of these figures are available online).

wide-field EUV imager SunCET (Mason et al., 2021), should help to fully characterize the capabilities of EUV imaging for CME detection and tracking.

Preliminary ECI data from these campaigns are available as special event data on the NCEI-hosted GOES-R Space Weather data page (<https://www.ngdc.noaa.gov/stp/satellite/goes-r.html>).

#### 4.2. Flare Dynamics/Evolution

Combined with its CCD's anti-blooming protection, SUVI's HDR imaging strategy (see Section 3.2.1) provides some specific advantages for observing large solar flares and eruptions. Many typical EUV imagers have been optimized to observe coronal loops or coronal holes, with flares only a secondary science target, and thus they have not prioritized clear images of extremely bright signals. Because a primary function of SUVI is to provide forecasters coronal context during flares and eruptions, it is important that SUVI deliver clear images of these events. Figure 18 shows a comparison of the 2017 September 10 X-flare observed by AIA and SUVI, revealing how even during the flare's impulsive phase, SUVI has a clear view of the flare and outgoing eruption (see Seaton & Darnel, 2018 for additional details).

In fact, analysis of several bright flares by SUVI indicates that, even for highly compact events, SUVI will observe up to X20-class flares without saturation or other artifacts in the field of view. Additionally, SUVI's HDR compositing strategy permits L2 images to capture both the bright flare and faint flare-associated features,

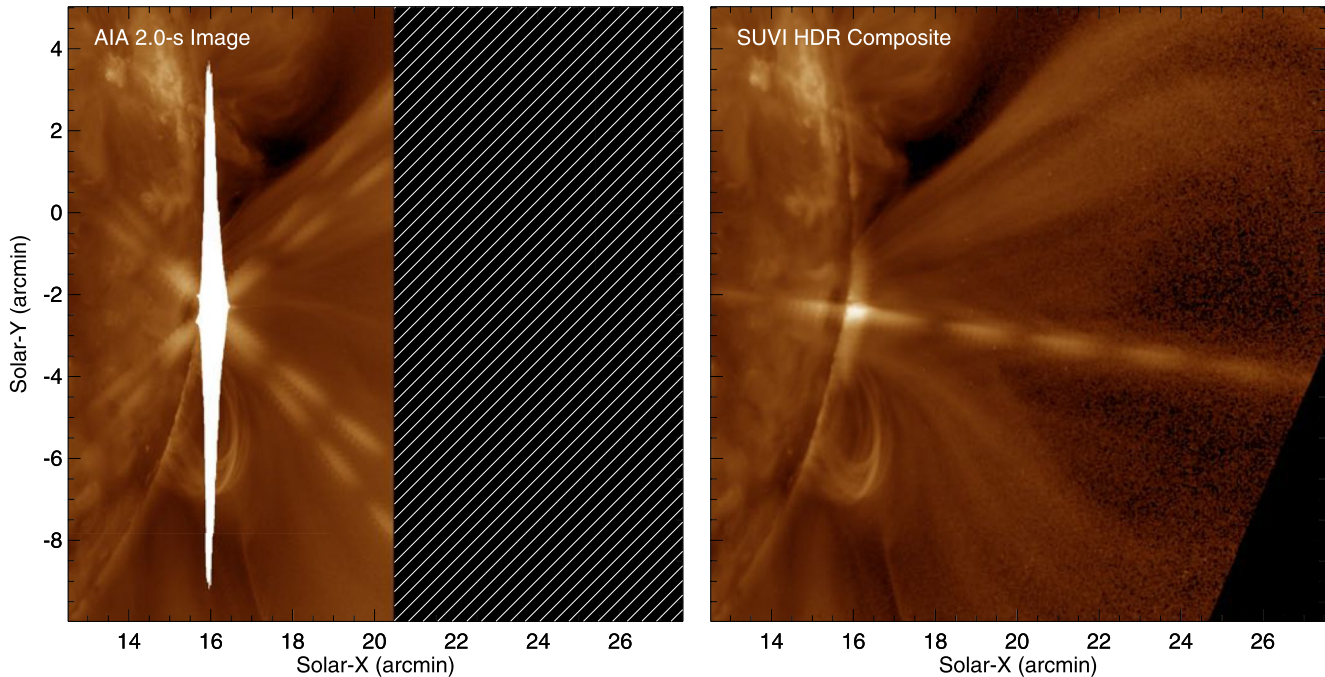


**Figure 18.** Simultaneous observations of the 2017 Sep 10 solar flare from Atmospheric Imaging Assembly (AIA)'s 193 Å channel (left) and Solar UltraViolet Imager (SUVI)'s 195 Å L2 composite image (right) show how SUVI's high dynamic range (HDR) strategy preserves detail over the full range of flare brightnesses with no loss of data to charge-coupled device blooming. SUVI's large field of view permits the tracking of flare-associated eruptions throughout most of their initial acceleration phase.

such as prominences, coronal dimmings, EUV waves, and erupting structures, within a single image frame. This capability can help forecasters better classify the global situation during the flare and potential flare-related impacts at Earth. It also provides highly complimentary data to that from other EUV and soft X-ray imagers for science analysis.

As of this writing, SUVI has observed only six X-class flares, four between 2017 September 6 and 10, one on 2021 July 3, and one on 2021 October 28, so its flare-observation capabilities have not yet been fully tested. SUVI observations have nonetheless proved instrumental to our understanding of the origins, solar effects, and space weather impacts of the September 10 event (e.g., Gopalswamy et al., 2018; Liu et al., 2019; Redmon et al., 2018; Seaton & Darnel, 2018; Veronig et al., 2018).

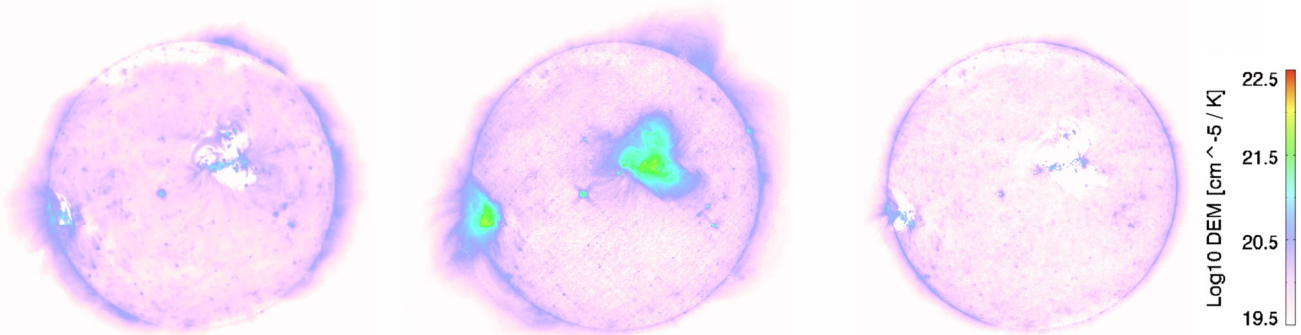
#### 4.3. Differential Emission Measures (DEM)

DEM inversions relate narrow-band EUV (and/or broadband X-ray) observations to the temperature and emission measure along the line of sight in the optically thin coronal plasma (Sylwester et al., 1980). DEM inversions are routinely used on AIA images with great success to create spatially resolved DEM maps of the solar corona used to infer the thermodynamic properties and evolution of spatially resolved coronal structures including active regions, coronal holes, and bright points (Hannah & Kontar, 2012a).

Accurately inverting for the thermodynamic properties of large solar flares using AIA images, however, remains limited due to saturation and blooming in flare pixels that compromises the accuracy of the DEM inversions (Cheung et al., 2015). Given the reduced pixel saturation and anti-blooming protection (see Sections 1.2.1 and 4.2), SUVI offers the potential to significantly improve the DEM inversion solutions during large solar flares.

SUVI measures optically thin coronal EUV emission in five channels (94, 131, 171, 195, and 284 Å), significantly overlapping those measured by AIA (94, 131, 171, 193, 211, and 335 Å) and encompassing plasma emission between  $5 \times 10^4$  and  $1 \times 10^8$  K (see Figure 1). Note that, as shown in Table 4, there is non-negligible contamination from He II emission in the 284 Å channel, so it is necessary either to remove this contamination

GOES 16 SUVI @ 2017-08-21T18:19



Emission Measure @  $\text{Log } T/K = [6.15, 6.25]$     Emission Measure @  $\text{Log } T/K = [6.35, 6.45]$     Emission Measure @  $\text{Log } T/K = [6.95, 7.05]$

**Figure 19.** Derived emission measure as a function of temperature using the sparse inversion solutions on Solar UltraViolet Imager (SUVI) images from 2017-08-21.

by subtracting an appropriately scaled 304 Å image or otherwise account for the presence of this optically thick contribution when computing a DEM including the 284 Å channel. Strategies to remove the 304 Å contribution to the 284 Å channel have been developed ([https://suvi.lmsal.com/Inst/Decoupling\\_284\\_and\\_304\\_images.html](https://suvi.lmsal.com/Inst/Decoupling_284_and_304_images.html)).

Most DEM inversion codes have been optimized to use AIA image data (e.g., Cheung et al., 2015; Hannah & Kontar, 2012; Plowman & Caspi, 2020). Given the overlap between the AIA and SUVI channels, modifying these codes to use SUVI data as input is relatively straightforward, and some preliminary tests have demonstrated this. For example, Figure 19 shows an example DEM derived using the sparse inversion code (Cheung et al., 2015) modified for SUVI data. Additional SUVI DEM tools are planned for the packages described in Section 3.4.

#### 4.4. Machine Learning

Machine learning (ML) algorithms require clean, calibrated data to perform optimally. Without carefully curated data, the ML algorithm may identify false patterns or outliers in the data and suggest incorrect conclusions or simply fail to converge to a stable ML model. SUVI has great potential for machine learning applications because of the long time baseline and the high stability of the data. The GOES-R series satellites will be operational through December 2040 with the possibility of future GOES satellites having instruments similar to SUVI. This long time baseline allows for machine learning studies over the entirety of the solar cycle. Additionally, there are rarely SUVI data gaps as multiple satellites are operational simultaneously. The multiplicity of observations from four nearly identical satellites allows for careful cross-calibration and curation of an AI-ready data set, much like Galvez et al. (2019) did for SDO data.

The SUVI thematic maps provide one example of the possibilities of machine learning using SUVI data. The thematic maps create a database of labeled solar phenomena that can be used to answer scientific questions such as “what is the average lifetime of a coronal hole?” or “how can we better understand and predict solar flares?”. As machine learning in solar physics advances, these maps will improve and become even more reliable.

## 5. Conclusion

NOAA's GOES-R series of satellites each host a EUV solar imager known as SUVI whose observations complement the observations currently available from other missions. The value of the observational and operational data set will largely be found in the extended and overlapping time period of the GOES-R mission, from 2016 to out beyond 2040. The overlapping observations from the primary and secondary GOES satellites not only provide operational redundancy but also ensure observational consistency between the two operational SUVI instruments. The design and hardware of the SUVI instruments has been described in detail, demonstrating a solid and time-proven design that shares many design characteristics with other instruments with which the

SUVI instruments share heritage. The on-ground calibration and on-orbit testing of the SUVI instrument has been described in detail, specifically drawing attention to innovations such as using the Boustrophedon scans to determine the instruments' flat fields. The performance characteristics, spectral and spatial, have been described to the best extent possible to accurately convey how the SUVI instruments observe solar phenomena. The SUVI data products have been described in detail along with location wherein to find those same products. Finally, we share some of the exciting opportunities that exist for utilizing the SUVI datasets, such as the Extended Coronal Imaging campaigns, DEM analysis, and the potential value for machine learning exploitation. In conclusion, the SUVI instruments aboard NOAA's GOES-R series of satellites are a great resource for both operational and research activities and needs.

### Conflict of Interest

The authors declare no conflicts of interest relevant to this study.

### Data Availability Statement

Solar UltraViolet Imager (SUVI) data is available from National Oceanic and Atmospheric Administration's National Centers for Environmental Information. Level-1b SUVI data products can be accessed via <https://doi.org/10.7289/V5FT8J93>. Level-2 and special campaign data can be accessed via <https://doi.org/10.25921/D60Q-G238>. SUVI software is available within the open-source repositories SolarSoft (IDL) and sunkit\_instruments (Python).

### Acknowledgments

Solar UltraViolet Imager (SUVI) product development, analysis, calibration, validation, and data stewardship by CIRES-affiliated authors within National Centers for Environmental Information (NCEI) was supported by National Oceanic and Atmospheric Administration cooperative agreement no. NA17OAR4320101. Some material in this paper was based upon work supported by the National Aeronautics and Space Administration under Grant No. 80NSSC20K1363. SUVI design, acquisition, and manufacturing, and testing by authors within LMSAL was supported by NASA GSFC (org: GOES-R/Code 417) under the "Solar UltraViolet Imager (SUVI)" program under contract number: NNG07HW20C. We thank our colleagues, present and past, in Boulder, including H. Bain, C. Clark, S. Codrescu, W. Denig, K. Hallock, S. Herring, V. Hsu, E. Kihn, L. Krista, J. Machol, R. Redmon, J. Rigler, W. Rowland, J. Rodriguez, D. Schmit, R. Steenburgh, M. Tilton, P. Wyatt for their efforts on behalf of the SUVI project and the NCEI Space Weather Team. We also thank G. Comeyne, J. Fulbright, S. Goodman, E. Kline, A. Krimchansky, D. Lindsay, M. Seybold, M. Shalcross, C. Smith, P. Sullivan, S. K. Tadikonda and the entire GOES-R Program Office for their support of the SUVI project. We thank P. Boerner and M. Cheung at Lockheed-Martin and F. Eparvier, A. Jones, M. Snow, and D. Woodraska, T. Woods of the Laboratory for Atmospheric and Space Physics for helpful discussions about instrument performance and analysis techniques.

### References

- Arge, C. N., & Pizzo, V. J. (2000). Improvement in the prediction of solar wind conditions using near-real time solar magnetic field updates. *Journal of Geophysical Research*, 105(A5), 10465–10480. <https://doi.org/10.1029/1999JA000262>
- Arp, U., Clark, C. W., Farrell, A. P., Fein, E., Furst, M. L., & Hagley, E. W. (2002). Synchrotron ultraviolet radiation facility SURF III. *Review of Scientific Instruments*, 73(3), 1674–1676. <https://doi.org/10.1063/1.1445833>
- Bein, B. M., Berkebile-Stoiser, S., Veronig, A. M., Temmer, M., Muhr, N., Kienreich, I., et al. (2011). Impulsive acceleration of coronal mass ejections. I. Statistics and coronal mass ejection source region characteristics. *The Astrophysical Journal*, 738(2), 191. <https://doi.org/10.1088/0004-637X/738/2/191>
- BenMoussa, A., Gissot, S., Schühle, U., Del Zanna, G., Auchère, F., Mekaoui, S., et al. (2013). On-orbit degradation of solar instruments. *Solar Physics*, 288(1), 389–434. <https://doi.org/10.1007/s11207-013-0290-z>
- Berthelot, D., & Gaudenchon, H. (1910). The chemical effects of ultraviolet rays on gaseous bodies - The effects of polymerisation. *Comptes Rendus*, 150.
- Boerner, P. F., Testa, P., Warren, H., Weber, M. A., & Schrijver, C. J. (2014). Photometric and thermal cross-calibration of solar EUV instruments. *Solar Physics*, 289(6), 2377–2397. <https://doi.org/10.1007/s11207-013-0452-z>
- Brueckner, G. E., Howard, R. A., Koomen, M. J., Korendyke, C. M., Michels, D. J., Moses, J. D., et al. (1995). The Large Angle Spectroscopic Coronagraph (LASCO). *Solar Physics*, 162(1–2), 357–402. <https://doi.org/10.1007/BF00733434>
- Chamberlin, P. C., Woods, T. N., & Eparvier, F. G. (2007). Flare Irradiance Spectral Model (FISM): Daily component algorithms and results. *Space Weather*, 5(7), S07005. <https://doi.org/10.1029/2007SW000316>
- Chamberlin, P. C., Woods, T. N., Eparvier, F. G., & Jones, A. R. (2009). Next generation X-ray sensor (XRS) for the NOAA GOES-R satellite series. In S. Fineschi, & J. A. Fennelly (Eds.), *Solar physics and space weather instrumentation III* (Vol. 7438, p. 743802). <https://doi.org/10.1117/12.826807>
- Cheung, M. C. M., Boerner, P., Schrijver, C. J., Testa, P., Chen, F., Peter, H., & Malanushenko, A. (2015). Thermal diagnostics with the atmospheric imaging assembly on board the solar dynamics observatory: A validated method for differential emission measure inversions. *The Astrophysical Journal*, 807(2), 143. <https://doi.org/10.1088/0004-637X/807/2/143>
- Dalrymple, N. E., Bianda, M., & Wiborg, P. H. (2003). Fast flat fields from scanning extended sources. *Publications of the Astronomical Society of the Pacific*, 115(807), 628–634. <https://doi.org/10.1086/374725>
- Delaboudiniere, J., Artzner, G., Brunad, J., Gabriel, J., Hochedez, J., Millier, F., et al. (1995). EIT: Extreme-ultraviolet Imaging Telescope for the SOHO mission. *Solar Physics*, 162(1–2), 291–312. <https://doi.org/10.1007/BF00733432>
- Dere, K. P., Del Zanna, G., Young, P. R., Landi, E., & Sutherland, R. S. (2019). CHIANTI—An atomic database for emission lines. XV. Version 9, improvements for the X-ray satellite lines. *The Astrophysical Journal Supplement Series*, 241(2), 22. <https://doi.org/10.3847/1538-4365/ab05cf>
- Eparvier, F., Crotser, D., Jones, A., McClintock, W., Snow, M., & Woods, T. (2009). The Extreme UltraViolet Sensor EUVS for GOES-R. *Proceedings of SPIE*, 7438. <https://doi.org/10.1117/12.826445>
- Freeland, S. L., & Handy, B. N. (1998). Data analysis with the SolarSoft system. *Solar Physics*, 182(2), 497–500. <https://doi.org/10.1023/A:1005038224881>
- Galvez, R., Fouhey, D. F., Jin, M., Szenicer, A., Muñoz-Jaramillo, A., Cheung, M. C. M., et al. (2019). A machine-learning data set prepared from the NASA Solar Dynamics Observatory Mission. *The Astrophysical Journal Supplement Series*, 242(1), 7. <https://doi.org/10.3847/1538-4365/ab1005>
- Gopalswamy, N., Yashiro, S., Mäkelä, P., Xie, H., Akiyama, S., & Monstein, C. (2018). Extreme kinematics of the 2017 September 10 solar eruption and the spectral characteristics of the associated energetic particles. *The Astrophysical Journal Letters*, 863(2), L39. <https://doi.org/10.3847/2041-8213/aad86c>

- Goryaev, F., Slemzin, V., Vainshtein, L., & Williams, D. R. (2014). Study of extreme-ultraviolet emission and properties of a coronal streamer from PROBA2/SWAP, Hinode/EIS and Mauna Loa Mk4 observations. *The Astrophysical Journal*, 781(2), 100. <https://doi.org/10.1088/0004-637X/781/2/100>
- Hannah, I. G., & Kontar, E. P. (2012). Differential emission measures from the regularized inversion of Hinode and SDO data. *Astronomy and Astrophysics*, 539, A146. <https://doi.org/10.1051/0004-6361/201117576>
- Hill, S. M., Pizzo, V. J., Balch, C. C., Biesecker, D. A., Bornmann, P., Hildner, E., et al. (2005). The NOAA GOES-12 Solar X-ray Imager (SXI) 1. Instrument, operations, and data. *Solar Physics*, 226(2), 255–281. <https://doi.org/10.1007/s11207-005-7416-x>
- Howard, R. A., Moses, J. D., Vourlidas, A., Newmark, J. S., Socker, D. G., Plunkett, S. P., et al. (2008). Sun Earth Connection Coronal and Heliospheric Investigation (SECCHI). *Space Science Reviews*, 136(1–4), 67–115. <https://doi.org/10.1007/s11214-008-9341-4>
- Hughes, J. M., Hsu, V. W., Seaton, D. B., Bain, H. M., Darnel, J. M., & Krista, L. (2019). Real-time solar image classification: Assessing spectral, pixel-based approaches. *Journal of Space Weather and Space Climate*, 9, A38. <https://doi.org/10.1051/swsc/2019036>
- Landi, E., Young, P. R., Dere, K. P., Del Zanna, G., & Mason, H. E. (2013). CHIANTI—An atomic database for emission lines. XIII. Soft X-ray improvements and other changes. *The Astrophysical Journal*, 763(2), 86. <https://doi.org/10.1088/0004-637X/763/2/86>
- Lemen, J. R., Title, A. M., Akin, D. J., Boerner, P. F., Chou, C., Drake, J. F., et al. (2012). The Atmospheric Imaging Assembly (AIA) on the Solar Dynamics Observatory (SDO). *Solar Physics*, 275(1–2), 17–40. <https://doi.org/10.1007/s11207-011-9776-8>
- Liu, Y. D., Zhu, B., & Zhao, X. (2019). Geometry, kinematics, and heliospheric impact of a large CME-driven shock in 2017 September. *The Astrophysical Journal*, 871(1), 8. <https://doi.org/10.3847/1538-4357/aaf425>
- Martínez-Galarce, D., Harvey, J., Bruner, M., Lemen, J., Gullikson, E., Soufli, R., et al. (2010). A novel forward-model technique for estimating EUV imaging performance: Design and analysis of the SUVI telescope. In M. Arnaud, S. S. Murray, & T. Takahashi (Eds.), *Space telescopes and instrumentation 2010: Ultraviolet to gamma ray* (Vol. 7732, p. 773237). <https://doi.org/10.1117/12.864577>
- Martínez-Galarce, D., Soufli, R., Windt, D. L., Bruner, M., Gullikson, E., Khatri, S., et al. (2013). Multisegmented, multilayer-coated mirrors for the solar ultraviolet imager. *Optical Engineering*, 52(9), 095102. <https://doi.org/10.1117/1.OE.52.9.095102>
- Mason, J. P., Chamberlin, P. C., Seaton, D., Burkepile, J., Colaninno, R., Dissauer, K., et al. (2021). SunCET: The Sun Coronal Ejection Tracker Concept. *Journal of Space Weather and Space Climate*, 11, 20. <https://doi.org/10.1051/swsc/2021004>
- O’Dwyer, B., Del Zanna, G., Mason, H. E., Weber, M. A., & Tripathi, D. (2010). SDO/AIA response to coronal hole, quiet Sun, active region, and flare plasma. *Astronomy & Astrophysics*, 521, A21. <https://doi.org/10.1051/0004-6361/201014872>
- O’Hara, J. P., Mierla, M., Podladchikova, O., D’Huys, E., & West, M. J. (2019). Exceptional extended field-of-view observations by PROBA2/SWAP on 2017 April 1 and 3. *The Astrophysical Journal*, 883(1), 59. <https://doi.org/10.3847/1538-4357/ab3b08>
- Plowman, J., & Caspi, A. (2020). A fast, simple, robust algorithm for coronal temperature reconstruction. *The Astrophysical Journal*, 905(1), 17. <https://doi.org/10.3847/1538-4357/abc260>
- Redmon, R. J., Seaton, D. B., Steenburgh, R., He, J., & Rodriguez, J. V. (2018). September 2017’s geoeffective space weather and impacts to Caribbean radio communications during hurricane response. *Space Weather*, 16(9), 1190–1201. <https://doi.org/10.1029/2018SW001897>
- Robbrecht, E., Berghmans, D., & Van der Linden, R. A. M. (2009). Automated LASCO CME catalog for solar cycle 23: Are CMEs scale invariant? *The Astrophysical Journal*, 691(2), 1222–1234. <https://doi.org/10.1088/0004-637X/691/2/1222>
- Rochus, P., Auchère, F., Berghmans, D., Harra, L., Schmutz, W., Schühle, U., et al. (2020). The solar orbiter EUI instrument: The Extreme Ultraviolet Imager. *Astronomy and Astrophysics*, 642, A8. <https://doi.org/10.1051/0004-6361/201936663>
- Schmelz, J. T., Reames, D. V., von Steiger, R., & Basu, S. (2012). Composition of the solar corona, solar wind, and solar energetic particles. *The Astrophysical Journal*, 755(1), 33. <https://doi.org/10.1088/0004-637X/755/1/33>
- Seaton, D. B., Berghmans, D., Nicula, B., Halain, J. P., De Groof, A., Thibert, T., et al. (2013). The SWAP EUV imaging telescope Part I: Instrument overview and pre-flight testing. *Solar Physics*, 286(1), 43–65. <https://doi.org/10.1007/s11207-012-0114-6>
- Seaton, D. B., & Darnel, J. M. (2018). Observations of an eruptive solar flare in the extended EUV solar corona. *The Astrophysical Journal Letters*, 852(1), L9. <https://doi.org/10.3847/2041-8213/aaa28e>
- Seaton, D. B., Darnel, J. M., Hsu, V., & Hughes, J. M. (2020). Chapter 18—Goes-R series solar dynamics. In S. J. Goodman, T. J. Schmit, J. Daniels, & R. J. Redmon (Eds.), *The GOES-R series* (pp. 219–232). Elsevier. Retrieved from <https://www.sciencedirect.com/science/article/pii/B9780128143278000184>
- Seaton, D. B., De Groof, A., Shearer, P., Berghmans, D., & Nicula, B. (2013). SWAP observations of the long-term, large-scale evolution of the extreme-ultraviolet solar corona. *The Astrophysical Journal*, 777(1), 72. <https://doi.org/10.1088/0004-637X/777/1/72>
- Seaton, D. B., Hughes, J. M., Tadikonda, S. K., Caspi, A., DeForest, C., Krimchansky, A., et al. (2021). *The Sun’s dynamic extended corona observed in extreme ultraviolet*. Nature Astronomy.
- Sylwester, J., Scrijver, J., & Mewe, R. (1980). Multitemperature analysis of solar X-ray line emission. *Solar Physics*, 67(2), 285–309. <https://doi.org/10.1007/BF00149808>
- Tadikonda, S. K., Freesland, D. C., Minor, R. R., Seaton, D. B., Comeyne, G. J., & Krimchansky, A. (2019). Coronal imaging with the Solar UltraViolet Imager. *Solar Physics*, 294(3), 28. <https://doi.org/10.1007/s11207-019-1411-0>
- Tarrio, C., Berg, R. F., Lucatorto, T. B., Eparvier, F. G., Jones, A. R., Templeman, B., et al. (2021). Evidence against carbonization of the thin-film filters of the extreme ultraviolet variability experiment onboard the Solar Dynamics Observatory. *Solar Physics*, 269(3), 55. <https://doi.org/10.1007/s11207-021-01806-4>
- The SunPy Community, Barnes, W. T., Bobra, M. G., Christe, S. D., Freij, N., Mumford, S., et al. (2020). The SunPy project: Open source development and status of the version 1.0 core package. *The Astrophysical Journal*, 890(1), 68. <https://doi.org/10.3847/1538-4357/ab477a>
- Veronig, A. M., Podladchikova, T., Dissauer, K., Temmer, M., Guo, J., Vrsnak, B., et al. (2018). Genesis and impulsive evolution of the 2017 September 10 coronal mass ejection. *The Astrophysical Journal*, 868(2), 107. <https://doi.org/10.3847/1538-4357/aaeac5>
- Woods, T. N., Eparvier, F. G., Hock, R., Jones, A. R., Woodraska, D., Judge, D., et al. (2012). Extreme Ultraviolet Variability Experiment (EVE) on the Solar Dynamics Observatory (SDO): Overview of science objectives, instrument design, data products, and model developments. *Solar Physics*, 275(1–2), 115–143. <https://doi.org/10.1007/s11207-009-9487-6>